ADVANCED MATERIALS TECHNOLOGIES
www.advmattechnol.de

Self-Gelling Quinone-Based Wearable Microbattery

*Thiago Bertaglia, Emily F. Kerr, Graziela C. Sedenho, Andrew A. Wong, Rafael N. P. Colombo, Lucyano J. A. Macedo, Rodrigo M. Iost, Luana C. I. Faria, Filipe C. D. A. Lima, Gabriel B. M. Teobaldo, Cristiano L. P. Oliveira, Michael J. Aziz, Roy G. Gordon, and Frank N. Crespilho**

Wearable power sources are envisioned since their development promises to speed up the widespread application of wearable devices in different areas, such as healthcare, smart-city management, and robotics. Here, the 4′-((9,10-anthraquinone-2-yl)oxy)butyrate (2-BEAQ), an anthraquinone derivative, is synthesized, and further applied for producing a redox-active shear-thinning hydrogel (BEAQ-gel). The gel comprises cylindrical aggregates of 2-BEAQ molecules dispersed within a water matrix, interconnected through ionic, ion-dipole, and hydrogen bonding interactions. BEAQ-gel also presents interesting rheological characteristics and composition tunability since it can be produced in a large range of concentrations. This improved redox 3D hierarchical network also makes the network capable of retaining high quantities of potassium hydroxide, thereby enhancing conductivity. By coupling BEAQ-gel with Ferricyanide the development of a wearable battery is demonstrated, which exhibits an output voltage of 0.89 V even when bent at a 180° angle, making it suitable for powering wearable devices. This work presents an innovative alternative for the production of wearable devices, from the design of the anode and cathode materials to the wearable casing and demonstrates the use of redox-active low-molecular-weight-gel (LMWG) as an active material of a microbattery giving a valuable glimpse to the further development of wearable energy storage devices.

1. Introduction

Smart textile-integrated microelectronic systems designed for wearable applications are rapidly advancing, with the potential to be worn by humans, animals, and machines.[1–3] The production of flexible microbatteries (MBs) poses a significant challenge for these systems. MBs are crucial for powering wearable devices, but achieving flexibility in their design has proven to be difficult. Common chemical compounds used in MBs, such as Zinc—carbon, Nickel-metal hydride, and Lithium-ion, offer advantages including high energy density, extended lifespan, and lightweight properties. However, adapting these materials to create flexible MBs requires overcoming technical hurdles related to their structural and electrochemical properties. Developing innovative, suitable materials and engineering approaches becomes essential to enable the manufacturing of flexible MBs, paving the way for advancements in flexible, wearable technologies.

T. Bertaglia, G. C. Sedenho[+], R. N. P. Colombo, L. J. A. Macedo, R. M. Iost, L. C. I. Faria, F. N. Crespilho
São Carlos Institute of Chemistry
University of São Paulo
São Carlos, São Paulo CEP 13566-590, Brazil
E-mail: frankcrespilho@iqsc.usp.br

E. F. Kerr, R. G. Gordon
Department of Chemistry and Chemical Biology
Harvard University
Cambridge, MA 02138, USA

A. A. Wong, M. J. Aziz
Harvard John A. Paulson School of Engineering and Applied Sciences
Harvard University
Cambridge, MA 02138, USA

F. C. D. A. Lima
Federal Institute of Education, Science, and Technology of São Paulo
Campus Matão
São Paulo 15991-502, Brazil

G. B. M. Teobaldo, C. L. P. Oliveira
Institute of Physics
University of São Paulo
São Paulo CEP 05508-090, Brazil

The ORCID identification number(s) for the author(s) of this article can be found under https://doi.org/10.1002/admt.202400623

[+]Present address: Department of Chemistry, Federal University of São Carlos (UFSCar), São Carlos, São Paulo CEP 13565-905, Brazil

DOI: 10.1002/admt.202400623

Among the challenges in developing MBs for wearable devices is the need to have adjustable mechanical properties, while delivering enough volumetric energy density and using non-toxic components.[4,5] In this scenario, the development of materials based on redox hydrogels with adjustable mechanical properties becomes an exciting strategy, since the chemical components employed can be non-toxic and do not cause health damage in case of leakage or accidents.[6] Hydrogels are semi-solid viscoelastic materials formed by 3D cross-liked networks that can absorb a large quantity of water.[7] Some hydrogels can resemble the soft-tissues of the human body,[8] and due to their key features, such as conductivity,[9] flexibility,[10] and stretchability,[11] they have been used as electrolytes in the development of aqueous flexible and stretchable batteries.[6]

Hydrogels can be synthesized by both chemical and/or physical routes. Chemical gels use common organic reactions, like free-radical polymerization,[12] condensation reactions,[13] and click-chemistry,[14] to produce new bonds between those precursor(s). Alternatively, the structure of the physical ones is maintained by physical interactions, such as hydrogen bonding,[15,16] and ionic interactions.[17] Furthermore, hydrogels can be obtained using polymer or low-molecular-weight-gelators, typically with molecular weight <1000 g mol^{-1}, as precursor materials. LMWGs are produced using nonpolymeric compounds that, through physical interactions and proper environmental conditions, aggregate in supramolecular structures, like fibrils, and form a 3D network capable of entrapping the solvent.[18,19] Although redox-active gels have proven to be suitable tools to enhance the performance of lithium sulfur batteries, there are scarce reorts in which they possess functions others than structural and water absorption/retention.[20] Also, the application of redox-active gelators leads to a higher volumetric capacity because it eliminates the dead volume occupied by non-redox active hierarchical structures. This functionality of redox-active compounds can lead to cost savings in manufacturing MBs and simplifying the battery design.

In this study, we introduce the development of an LMWG functioning as a redox-active material in MBs. To the best of our knowledge, while LMWGs have been utilized in batteries, they typically play a supporting role, and there is no existing report of LWMGs acting as the primary redox-active material in batteries. We present the synthesis and application of a anthraquinone derivative, 4-((9,10-dioxo-9,10-dihydroanthracen-2-yl)oxy)butanoic acid (2-BEAQ), which readily forms a redox LMWG when dissolved in KOH solution (BEAQ-gel). The hydrogel is easily obtained by handling the concentration of 2-BEAQ in the aqueous 1.0 mol L^{-1} KOH solution, without the need for any additives, as 2-BEAQ exhibits self-gelling properties. The synthesized hydrogel displays electroactivity and exhibits shear-thinning behavior while being stable at higher temperatures than that usually found for the body of a healthy person. As a proof-of-concept, we pair BEAQ-gel with ferricyanide as the other half-cell reactant, resulting in an organic solvent-free and flexible wearable microbattery. The microbattery shows a high open circuit voltage of 0.89 V even being bent at 180° and enough volumetric power for meet the requirements of low-consumption wearable devices. Thus, this work intends to broaden the scope of active materials for the new generation of flexible and wearable energy storage devices by developing a new battery as a whole, from the flexible casing to the active material synthesis, characterization, and application.

2. Results and Discussion

2.1. 2-BEAQ and BEAQ-Gel: Electrochemical and Spectroelectrochemical Characterization

2-BEAQ is an anthraquinone derivative having ether and carboxylic acid side groups attached to the anthraquinone core (Figure S1a, Supporting Information). The synthesis was carried out in three steps using 2-hydroxyanthraquinone as precursor. First, 2-hydroxyanthraquinone performs a nucleophilic substitution in ethyl-4-bromobutyrate. The product is submitted to alkaline ester hydrolysis followed by acidification with hydrochloric acid, to finally obtain 2-BEAQ (see all synthesis details in the Supporting Information). 2-BEAQ structure was confirmed by ^{1}H NMR (Figure S1c, Supporting Information).

At room temperature, 2-BEAQ is a light-green solid (Figure S1b, Supporting Information) soluble in 1.0 mol L^{-1} KOH. Even though 2-BEAQ is a relatively small molecule, it shows a critical concentration point where it begins to self-gel, that is, a phase transition from liquid to gel occurs, which will be detailed later. In solution, 2-BEAQ undergoes a quasi-reversible redox process (**Figure 1a**) involving two electrons and with peak separation and half-wave potential ($E_{1/2}$) equal to 35 mV (at 5 mV s^{-1}) and −0.66 V, respectively, as evidenced by the cyclic voltammograms (CVs) in Figure 1a and Table S1 (Supporting Information). Rotating-disk electrode measurements (Figure S2a, Supporting Information) in 2-BEAQ solution evidence that the steady-state current increases with the increase of the rotation rate, and the Levich plot (Figure S2b, Supporting Information) indicates a diffusion coefficient (D) of 3.04×10^{-6} cm^2 s^{-1} in 1.0 mol L^{-1} KOH (Sections 1.5 and 4, Supporting Information). CVs of 2-BEAQ in different pH conditions (Figure 1b) show a shift in the $E_{1/2}$ value within pH 8.0 and 12.0, evidencing a proton-coupled-electron-transfer. The Pourbaix diagram (Figure 1c) constructed from the CVs exhibits two main linear regions with different slopes. From pH 8.0 to 12.5, the slope of -37 mV pH^{-1} indicates a one-proton two-electron ($1H^+/2e^-$) reaction (Equations S3 and S4, Supporting Information). In contrast, in highly alkaline conditions (pH > 12.5), $E_{1/2}$ does not significantly change (−4 mV pH^{-1}), indicating that there is no proton involved in the redox reaction above pH 12.5. The 2-BEAQ electrochemical reaction is described in Figure S3 (Supporting Information), indicating $1H^+/2e^-$ and $0H^+/2e^-$ reactions, according to the pH condition. Approximating the pK_a of 2-BEAQ carboxylic acid to that obtained for butyric acid (4.82), we will expect all 2-BEAQ molecules to be deprotonated in the studied conditions. Therefore, fully reduced 2-BEAQ species are doubly (2-BEAQH^{2-}) and triply (2-BEAQ^{3-}) negatively charged from pH 8 to 12.5 and from pH 12.5 to 14.0. Both $E_{1/2}$ and D values obtained for 2-BEAQ are comparable with values obtained for some viologen-[10] and anthraquinone-[21] based compounds (Table S2, Supporting Information).

UV–vis spectroelectrochemical measurements (Figure 1d–i) of 5 mmol L^{-1} 2-BEAQ in 1.0 mol L^{-1} KOH solution were performed to investigate its redox mechanism. Successive potentials between −0.90 V (reduced state) to −0.30 V (oxidized state) were applied to the electrode. The spectrum recorded at −0.90 V

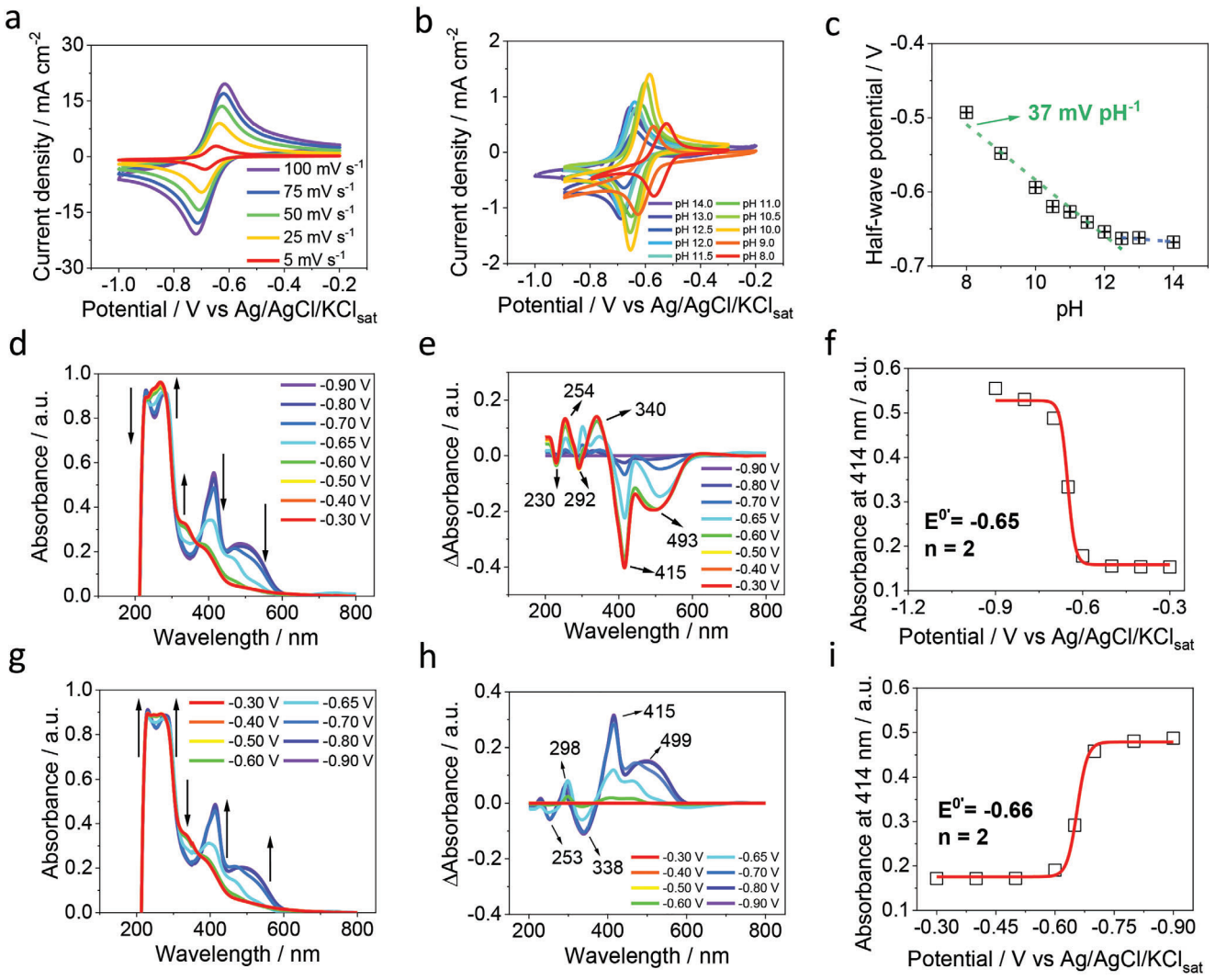

Figure 1. a) CVs of 1.0 mmol L^{-1} 2-BEAQ in 1.0 mol L^{-1} KOH from 100 to 5 mV s^{-1} recorded with flexible carbon fiber (FCF) electrode. b) CVs of 1.0 mmol L^{-1} 2-BEAQ recorded at pHs ranging from 8.0 to 14.0 using FCF as working electrode at 5 mV s^{-1}. c) Dependence of $E_{1/2}$ with the pH of the 1.0 mmol L^{-1} 2-BEAQ solution. d) UV–vis spectra recorded in 1.0 mmol L^{-1} 2-BEAQ solution at different applied potentials ranging from −0.90 to −0.30 V. e) Absorbance difference between the obtained spectra at different applied potentials and at −0.90 V. f) Evolution of the absorbance at 414 nm with the applied potential in the oxidation scan. g) UV–vis spectra recorded in 1.0 mmol L^{-1} 2-BEAQ solution at different applied potentials ranging from −0.30 to −0.90 V. h) Absorbance difference between the obtained spectra at different potentials and at −0.30 V. i) Evolution of absorbance at 414 nm with the applied potential in the reduction scan. All measurements were performed at room temperature.

(Figure 1d, purple line) shows two intense bands at 414 and 485 nm assigned to 2-BEAQH^{2-}.[22] These species are created by the abstraction of protons, which are generated as a result of electrode polarization. The pH alteration in areas near the electrode surface has been confirmed in alkaline media,[23] and we propose that this phenomenon is also taking place on the FCF surface. The intensity of these bands clearly decreases when the applied potential is less negative and disappear at −0.30 V. At −0.30 V, the spectrum shows absorption bands at 325 and 384 nm attributed to $\pi \rightarrow \pi^*$ of C=C benzenoid structure and $n \rightarrow \pi^*$ transition of carbonyl groups, similarly to the spectrum of the fresh 2-BEAQ solution (before potential application) (Figure S4, Supporting Information).[24] The differential UV–vis spectra (Figure 1e) shows the consumption of 2-BEAQH^{-2} when the potential is less negative, as the bands at 415 and 493 nm decrease in intensity. The absorption band at 340 nm arises from 2-BEAQ molecules and indicates the oxidation process is taking place. This absorption feature originally occurs at 326 nm for anthraquinone (9,10-anthracenedione) dissolved in DMF.[25] However it is well known that polar solvents can cause a redshift in absorption bands of anthraquinones due to the formation of hydrogen bonding,[26] which explains the wavelength difference from 2-BEAQ to this parent compound. A negative signal at 292 nm indicates the consumption of 2-BEAQ$^{\bullet-}$ at less negative potentials and corroborates with the formation of oxidized anthraquinone molecules in solution. The bands at 254 and 230 nm are assigned to $\pi \rightarrow \pi^*$ of the benzenoid chromophore of 2-BEAQ.[27] Figure 1f shows the dependence of the absorbance at 414 nm with the applied

potential in the reduction scan. This signal is attributed to 2-BEAQH^{2-} species and its monitoring gives valuable information about the electrochemical process taking place. It demonstrates the studied electrochemical process has a Nernstian behavior giving $E_{1/2}$ equal to −0.65 V and 2 electrons. Figure 1g,h shows the recorded spectra and absorbance difference according to the applied potentials in the reduction scan. The absorptions at 298, 415, and 499 nm are assigned to the formation of the 2-BEAQ$^{\bullet-}$ and 2-BEAQH^{2-}, respectively. The consumption of oxidized anthraquinone molecules can be observed in the negative band at 338 nm, which indicates that electrochemical reduction is taking place. The signal at 253 nm represents a $\pi \rightarrow \pi^*$ transition of benzenoid character. Figure 1i shows the dependence of the absorbance at 414 nm with the applied potential and gives $E_{1/2}$ and n values close to the oxidation scan and those obtained from the CV and Pourbaix diagram. In summary, UV–vis spectroelectrochemistry confirms the quasi-reversible electrochemistry oxidation/reduction of 2-BEAQ with a $2e^-/1H^+$ mechanism in alkaline conditions.

2.2. BEAQ-Gel: Structure and Properties

Despite the fact that 2-BEAQ has been already reported for producing sensors,[28–30] its intriguing property of self-gelling has not been explored so far. In this section, we thoroughly analyzed and discussed this remarkable behavior since it has important outcomes for the energy storage and conversion field, such as the development of novel redox-active self-gelling molecules for semisolid batteries[31] and the application of redox hydrogels as a protection layer for sensitive (bio)catalysts.[32] Indeed, it is the first report of a very simple anthraquinone acting as a low-molecular-weight gelator, to the best of our knowledge. Thus, a careful understanding of this remarkable behavior is indispensable both from the fundamental and applied point-of-view.

A phase transition occurs when a 2-BEAQ solution transforms into a gel, forming a stable BEAQ hydrogel at room temperature called BEAQ-gel. Notably, hydrogel formation is observed only at 2-BEAQ concentrations as low as 0.7% (w/v), as depicted in Figure S5 (Supporting Information). This highlights the versatility of gel production, as the hydrogel can be readily obtained at room temperature by controlling the concentration of 2-BEAQ. Furthermore, we noticed that at the same concentration, 2-BEAQ is insoluble in 1.0 mol L^{-1} NaOH, forming a turbid green suspension (Figure S6, Supporting Information), despite the pH and ionic strength of 1.0 mol L^{-1} NaOH being similar to 1.0 mol L^{-1} KOH. The difference between these solutions can be attributed to the size of their cations, as the ionic radii of hydrated potassium and sodium ions are of 2.70 and 2.38 Å, respectively.[33] This finding indicates that the phase transition of 2-BEAQ is ionic-driven, and that 2-BEAQ interacts more effectively with larger cations, such as potassium, which facilitates the formation of BEAQ-gel. We conducted experiments to investigate the electrochemical properties of BEAQ-gel, as shown in **Figure 2a**. The results indicate a quasi-reversible electrochemical reaction with an $E_{1/2}$ value comparable to that obtained in solution. As expected, there is a decrease in the ratio between the anodic and cathodic peak current densities (j_{pa}/j_{pc}) for BEAQ-gel (Table S3, Supporting Information) in comparison with the results obtained in solution (Table S1, Supporting Information), which suggests differences in the kinetics of electron transfer in gel phase. This could be due to the 3D gel structure, which could affect the diffusion of the redox-active species and hinder electron transfer kinetics. Despite the observed differences in electron transfer kinetics, the BEAQ-gel still exhibited excellent electroactivity and low resistance, as will be further discussed in the next section.

The mechanical and morphological properties of BEAQ-gel were characterized through rheological and spectroscopic measurements. The obtained mechanical spectrum of BEAQ-gel at varying temperatures is presented in Figure 2b. The results demonstrate a significant influence of temperature on both the storage (G') and loss (G'') moduli, with their values decreasing as temperature increases. Notably, G' values remain higher than G″ across all studied temperatures, indicating the stable solid behavior of BEAQ-gel. Importantly, the gel stability was maintained even at 45 °C, a temperature much higher than that typically found in the human body under normal conditions. This suggests that even with direct contact with the user's skin for extended periods, there is no risk of sol–gel transition occurring within the battery. However, G″ is only one order of magnitude higher than G' indicating the liquid behavior is also important in the material. This behavior is clearly observed in Figure S7 (Supporting Information) which presents a sol–gel transition of BEAQ-gel since G′ becomes higher than G″ in all studied temperatures. This transition value is temperature-dependent and decreases as the temperature increases, suggesting higher mobility of 2-BEAQ molecules inside the gel at high temperatures. Also, the rheological data suggests BEAQ-gel can be considered a weak-gel, a marked characteristic of gels that have physical interactions as the main driving force. We will show later in this section this behavior is corroborated by spectroscopic and x-ray scattering data. These findings highlight the potential of BEAQ-gel as a stable and reliable material for use in MBs.

The interaction between cations and oxygen-containing functional groups, such as C═O and COOH or COO$^-$, is a well-known phenomenon that can cause a shift in the material's infrared absorptions, indicating a change in its molecular arrangement. Taking advantage of this high sensitivity to molecular modifications, we employed Fourier transform infrared spectroscopy (FTIR) to investigate the microstructure of BEAQ-gel. Our analysis involved comparing the spectra of 2-BEAQ powder, freeze-dried BEAQ-gel (K-BEAQ), and BEAQ-gel synthesized in D_2O (D_2O-K-BEAQ-gel), as illustrated in Figure S8 (Supporting Information) and Figure 2c. The 2-BEAQ powder spectrum exhibited all the expected absorptions, including the anthraquinone moiety, carboxylic acid, and ether functional groups (Table S4, Supporting Information). Despite the absorption bands of D_2O, there were only slight differences observed between the K-BEAQ, D_2O-K-BEAQ-gel, and 2-BEAQ powder spectra, without any indication of the emergence or disappearance of absorption signals, which could suggest the formation or breakage of chemical bonds. This outcome indicates that the BEAQ-gel hierarchical network is maintained by intermolecular interactions, which is consistent with the thermo-reversible behavior of the BEAQ-gel (Video S1, Supporting Information) and the earlier findings regarding the essential role of potassium ions in the hydrogel formation. The absorption signal related to C═O stretching vibration at 1711 cm^{-1} in the 2-BEAQ powder spectrum disappears

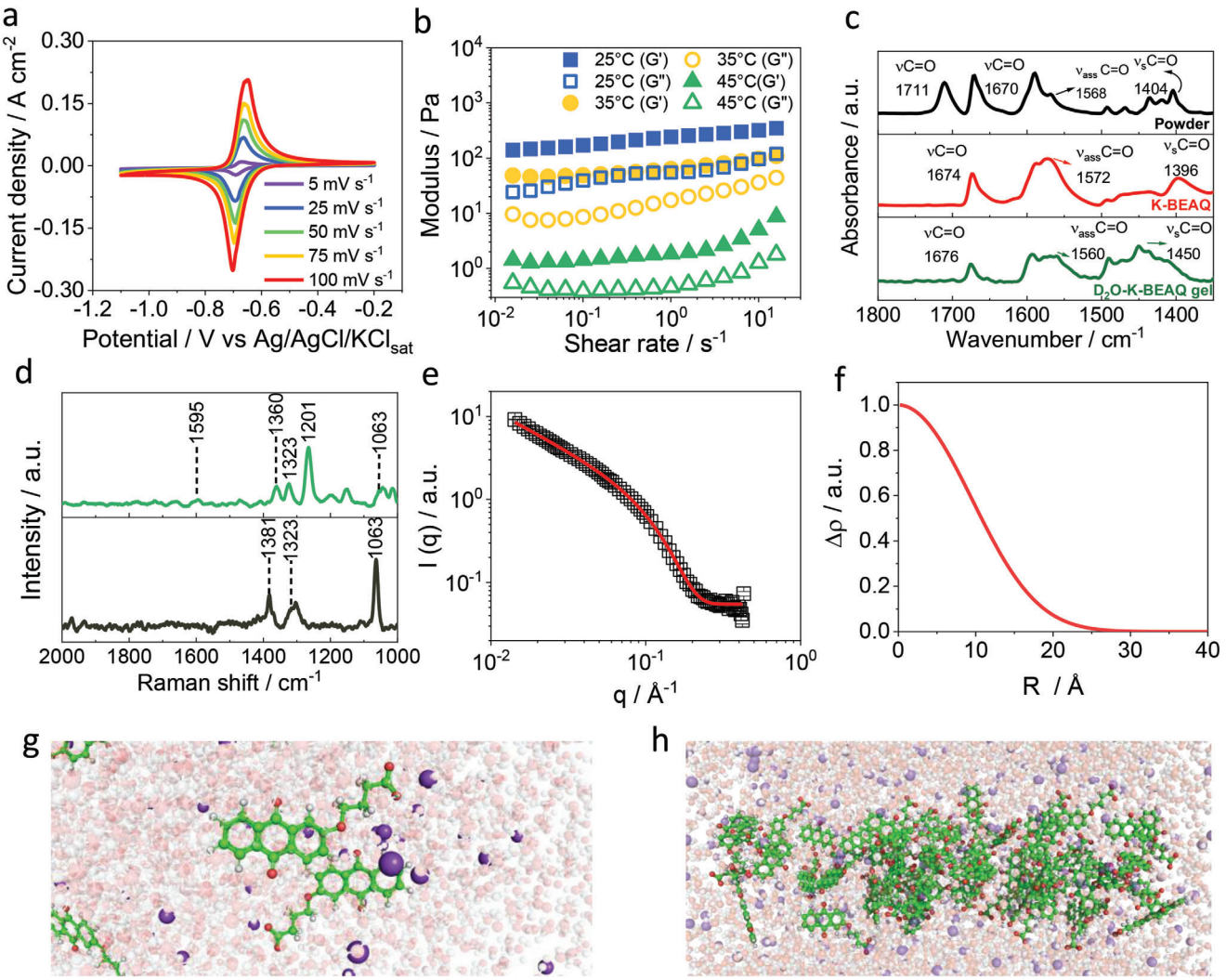

Figure 2. a) CVs of BEAQ-gel at different scan rates using FCF as working electrode. An ohmic drop correction of 14 Ω was considered. b) Mechanical spectra of 3% (w/v) BEAQ-gel at different temperatures. c) FTIR spectra of 2-BEAQ powder, K-BEAQ, and D_2O-K-BEAQ-gel showing wavenumbers from 1350 to 1800 cm^{-1}. d) Raman spectra of K-BEAQ (green) and D_2O-K-BEAQ-gel (black), e) SAXS data for 1.5% (w/v) BEAQ-gel. The red line indicates the fitting of diffuse cylinder model. f) Hankel transform of the SAXS data showing the electron density profile according to cylinder's radius. g) simulation of BEAQ solution and h) simulation of 1.5% (w/v) BEAQ-gel structure using a packing approach based on BOX-QUACAN method. The green, purple, white, and red spheres represent carbon, potassium, oxygen, and hydrogen atoms respectively. Water molecules and hydroxide ions are translucent aiming a facile visualization of the interactions between 2-BEAQ and potassium ions.

and the signals pertaining to the carboxylate group increase in K-BEAQ and D_2O-K-BEAQ-gel samples. The carboxylate absorption modes appear at 1572 ($\nu_{ass,\ COO^-}$) and 1396 cm^{-1} ($\nu_{s,\ COO^-}$) for K-BEAQ, and at 1560 ($\nu_{ass,\ COO^-}$) and 1450 cm^{-1} ($\nu_{s,\ COO^-}$) for D_2O-K-BEAQ-gel, as highlighted in Figure 2c. These results indicate the gel is formed by 2-BEAQ carboxylate form (2-BEAQ-COO^-). At the studied conditions, the proton is practically absent, which results in 2-BEAQ-COO^- having potassium ion as its counter-ion. The absorption related to 9,10-anthraquinone (C═O) moiety is observed at a higher wavenumber for K-BEAQ and D_2O-K-BEAQ-gel in comparison to 2-BEAQ powder, indicating an ion-dipole interaction between the anthraquinone and dissociated potassium hydroxide. These observations support the idea that 2-BEAQ undergoes an ionic-driven gelation process where the dissociated potassium ion plays a critical role. A similar behavior was already reported in the literature for naphthalene-functionalized dipeptides.[18] At high pH, these compounds form viscous solutions containing supramolecular structures that, entangle and forms a stable gel at room temperature upon adding alkali and alkaline earth metal ions.[18,34]

The Raman vibrational spectroscopy investigation was undertaken to determine the chemical structure of the self-gelling compound 2-BEAQ and the growth patterns of the gel of both K-BEAQ and D_2O-K-BEAQ. Figure 2d shows the Raman spectra of K-BEAQ and D_2O-K-BEAQ-gel in its deprotonated molecular state, as investigated previously using FTIR. In Figure 2d, the peak at 1360 cm^{-1} is attributed to C═O stretching band for K-BEAQ and shifts toward 1381 cm^{-1} for D_2O-K-BEAQ. This result is consistent with our previous findings since we observed an interaction between COO^- and K^+, which can act as the

driving force for bond length increasing. The appearance of a strong stretching band at 1201 and 1323 cm^{-1} is attributed to intra-ring stretches, 1595 cm^{-1} is attributed to C═C of phenyl stretching rings, and 1063 cm^{-1} is attributed to C—C stretching.

There is strong evidence to support the proposition that the interaction between 2-BEAQ and potassium ions leads to the formation of organized supramolecular structures. To investigate this, we conducted small-angle X-ray scattering (SAXS) measurements. Our proposed model for the BEAQ-gel structure suggests that 2-BEAQ-COO^- chelates potassium ions, and these potassium ions interact with the carbonyl moiety of 9,10-anthraquinone, resulting in the formation of a 3D hierarchical network in the BEAQ-gel. Figure 2g and Figure S9 (Supporting Information) depict the 3D molecular arrangement, designed using the PackMol software,[35] of the BEAQ-gel structure. 2-BEAQ molecules are not equally distributed pattern over the cube structure (Figure S9, Supporting Information), indicating they tend to aggregate and form supramolecular structures. Potassium ions are found near 2-BEAQ molecules (Figure 2g), corroborating our FTIR results regarding to the strong coulombic and ion-dipole interactions between 2-BEAQ and K^+ cations. From the theoretical perspective, the assess volume of K^+ has less constraints to be packed ≈2-BEAQ. These findings provide compelling support for the idea that 2-BEAQ forms organized supramolecular structures through aggregation in solution. It is noteworthy that both carboxylate and 9,10-anthraquinone can form hydrogen bonds with water molecules, which are essential for maintaining the BEAQ-gel structure. While ionic and ion-dipole interactions such as 2-BEAQ-COO^-K^+ and $C{=}O^{\delta-}K^+$ are stronger, hydrogen bonding is much more numerous. At a concentration of 1.50% (w/v), the BEAQ-gel stoichiometry is 1110:20:19:1 (H_2O:K^+:OH^-:2-BEAQ-COO^-), which indicates a considerable excess of water molecules. The excess of water, along with ion-dipole interactions with potassium ions and hydrogen bonding with 2-BEAQ and water, enables the formation of a 3D stable network that can absorb and retain water.

A cylinder model with a diffuse external interface was employed to fit the SAXS data (Figure 2e). Further information about the model can be found in (Section 1.12, Supporting Information). The SAXS data indicates 2-BEAQ aggregates in solution forming diffuse cylinders a with radius of 11.8 Å ± 0.8 Å and a diffuse interface of 6.2 Å ± 0.6 Å. A rough estimation shows the cylinder length is ≈6000 Å ± 1500 Å. The Hankel transform of the scattering data shows the electron density of a cylindrical structure according to their radius. The obtained radial electron density profile (Figure 2f) of the 2-BEAQ-COO^- cylinders provides valuable insights into their internal structure. The non-hollow nature of these cylinders, characterized by a higher density at the center and a radial decrease, indicates a unique arrangement of electrons within the material. This density profile suggests a more compact core, potentially containing a higher concentration of 2-BEAQ molecules or other components, surrounded by a progressively less dense outer region. A model of a cylindrical structure was constructed using the parameters obtained from SAXS analysis (Figure 2h). This model was generated using the PackMol software, simulating the packing of molecules within the cylindrical framework. By incorporating the SAXS-derived parameters, such as the size, shape, and electron density distribution obtained from the scattering data, we were able to create a representative model that closely mimics the experimental observations.

To understand the influence of 2-BEAQ concentration on the supramolecular structure form and size, we extended the SAXS measurements to BEAQ-gels with concentrations of 0.7, 3.00, and 4.50% (w/v) (Figure S10a, Supporting Information). All SAXS data well fit the previously employed diffuse cylinder model and only slight changes in the cylinder radius were observed according to the gel concentration (see Table S5, Supporting Information). Nonetheless, the radius of all obtained cylinders lies ≈18 Å, which is the value obtained for 1.50% (w/v) BEAQ-gel. From the Hankel transform of the scattering amplitude of the cylinder cross section one obtains the radial electron density profiles (Figure S10b, Supporting Information), which indicates the cylinder are dense with a higher 2-BEAQ concentration at the core, as obtained for 1.50% (w/v) BEAQ-gel. Even though the model fitted indicates the cylinders in all samples are very long, the 2-BEAQ concentration influences the cylinder's length (see Table S5, Supporting Information). Higher 2-BEAQ concentration leads to shorter cylinders, indicating a higher degree of cross linking in the gel. This result suggests the BEAQ-gel at higher concentrations, such as 3.00 and 4.50% (w/v), probably have a G″ higher than those at lower concentrations, implying a direct relationship between the gel concentration and their rheological solid behavior. The interaction parameter (ν) was significant for the 3.00% (w/v) and 4.50% (w/v) samples, implying an interaction between the cylinders, possibly due to higher concentration. Conversely, the 0.7 (w/v) and 1.50% (w/v) samples exhibited no interaction between the cylinders due to lower concentrations ($\nu = 0$). Finally, the calculated polydispersity for all structures was lower than 1%.

We further investigated the microstructure of BEAQ-gel with scanning electron microscopy (SEM) aiming to have a deeper clue about the self-assembly of the BEAQ-cylinders. **Figure 3a–d** shows SEM micrographs with different magnifications and 2-BEAQ concentrations. LMWGs form through the self-assembly of the free molecules in supramolecular structures which interact with each other forming larger structures, like fibrils. Finally, these fibrils entangle with their neighborhood and form the 3D hierarchical structure of the gel. Figure 3a shows the fibrils formed due to the BEAQ-gel cylinder's aggregation and illustrates the hierarchical 3D network of BEAQ-gel. As expected for an amorphous material, there is no patterned arrangement of those fibrils over the whole sample. Figure 3b,c shows a closer view of the fibrils entanglement where we observe the fibrils interact with its whole neighborhood giving rise to a well-packed and dense material, which again demonstrates the remarkable self-gelling property of 2-BEAQ. Figure 3b,c also shows the presence of pores with different sizes in the structure of BEAQ-gel, where possibly the diffusion of the molecules and ions takes place. Figure 3d shows a micrograph of BEAQ-gel in higher concentration and displays fibrils with a much less sharp but higher content of material on their surface, which indicates the fibrils tend to agglomerate forming thinker structures despite forming new ones. This finding is in accordance with the previous SAXS data obtained since it has shown that the cylinders interact with each other in higher concentrations. It is noteworthy the pores are not spread over the whole surface of BEAQ-gel, which corroborates with our previous findings about the constraints in the

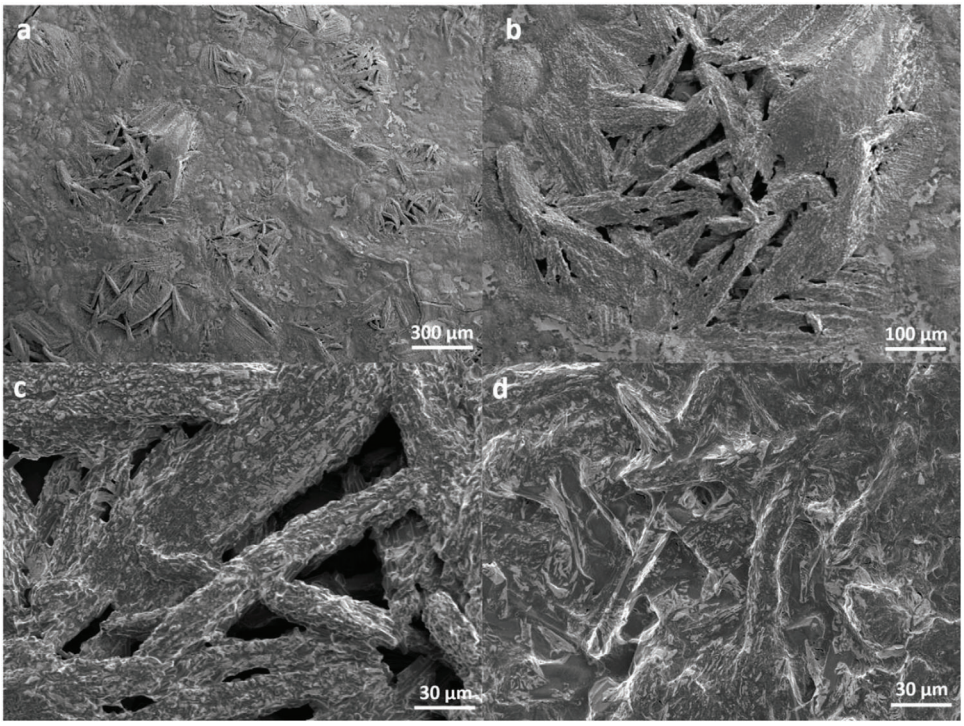

Figure 3. Scanning electron micrographs of a–c) 0.7% (w/v) and d) 1.5%(w/v) BEAQ-gel.

diffusion through the gel. However, as we stated earlier BEAQ-gel is obtained by controlling 2-BEAQ concentration, which means much more porous hydrogel can be obtained through careful structural and optimization, which lies out of the scope of this work.

The spectroscopic, SAXS, and SEM characterization of the BEAQ-gel provided valuable insights into its structural properties and the mechanisms underlying the gel formation. The gel primarily consists of 2-BEAQ-COO^- with potassium ions as counter-ions, and the absence of protons supports this composition. The absorption observed at a higher wavenumber in the gel samples compared to the 2-BEAQ powder indicates an ion-dipole interaction between the anthraquinone and dissociated potassium hydroxide. This suggests that the gel formation process is driven by ionic interactions, with the dissociated potassium ion playing a crucial role. Molecular simulations provide visual insights of 2-BEAQ-COO^- molecules aggregation and possible supramolecular structures in solution, depicting a 3D network capable of imbibing water. The stoichiometry of the BEAQ-gel indicates a significant excess of water molecules, along with the presence of potassium and hydroxide ions. The structural analysis using SAXS reveals that the cylindrical structures of the BEAQ-gel provide a large surface area for electrochemical reactions in flexible MBs. The smooth transition in the diffuse interface between the cylinders core and the surrounding solvent suggests a well-defined structure. The results demonstrate a relatively narrow distribution of cylindrical particles with low polydispersity. The length of the cylinders varies among the samples, with higher concentrations leading to stronger interactions. This suggests that the behavior of the gel may depend on its concentration. The SEM micrographs corroborates with both SAXS and simulation results as it shows the tendency of 2-BEAQ to self-assemble forming fibrils that further interact giving rise the 3D hierarchical network of the gel. Overall, these findings highlight the potential application of the BEAQ-gel as an anodic component in flexible MBs, owing to its unique structural properties and ability to facilitate electrochemical reactions and ion exchange with the alkaline electrolyte.

2.3. Wearable Microbattery Based on BEAQ-Gel

Organic molecules are promising active compounds for batteries since they show fast electrochemical reactions, structure tunability, and interesting electrochemical potentials for producing aqueous batteries.[36] Despite the fact that organic molecules have been extensively used in the field of redox-flow batteries, only little efforts have been paid in the application of organic active compounds in microbatteries.[31] Thus, to prove the feasibility of using 2-BEAQ, we employed it as the anode material and paired it with ferricyanide as the cathode material in a wearable MB configuration. This battery achieved an impressive voltage output of 0.89 V, delivering substantial power capacity suitable for the efficient operation of wearable devices. To minimize the exposure of the hydrogels to light and air, we developed a flexible casing structure before assembling the MB. This casing can be easily bent and stretched, making it suitable for wearable applications. We then assembled a wearable MB, using BEAQ-gel as the anode, ferricyanide incorporated in xanthan gum (Ferricyanide-XG-gel) as the cathode, and Nafion 212 membrane as the separator, as shown in the exploded view in **Figure** 4a. The MB was assembled by transferring 250 µL of each gel into the casing pieces and

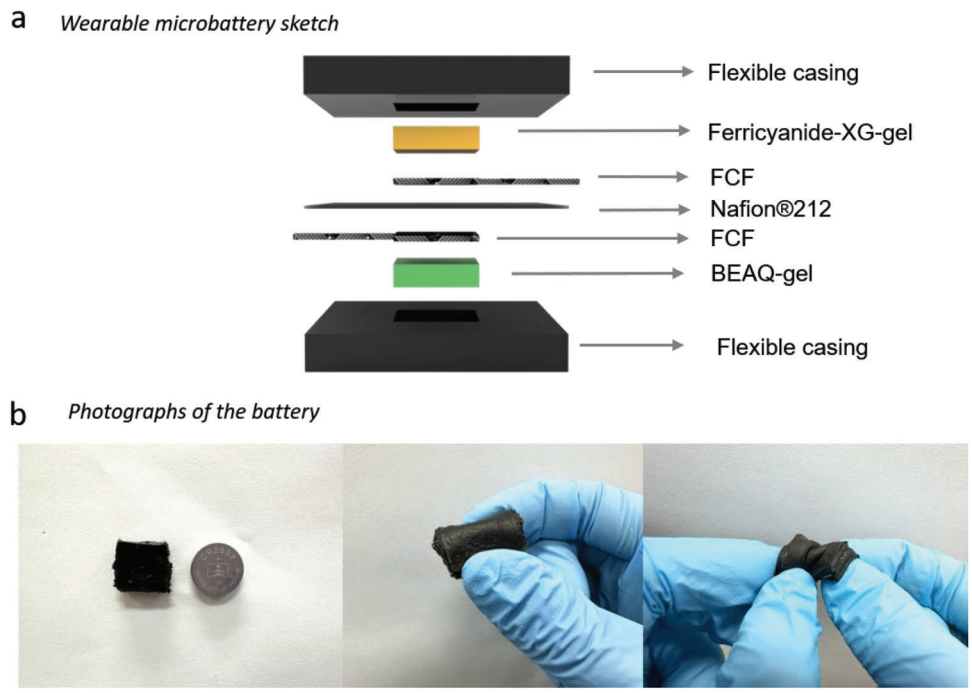

Figure 4. a) 3D sketch of the developed wearable microbattey and b) images of the battery under comparison with a CR2032 commercial battery, bending, and torning.

adding an FCF-based current collector at the top of each chamber. The MB was then closed with silicon acetic resin and left to rest overnight. XG is a natural polysaccharide derived from *Xanthomonas sp*. (see molecular structure in Figure S11a, Supporting Information). It is biocompatible, inexpensive, an efficient thickener, and can endure a wide pH range. Moreover, XG has been reported for the production of electrolytes for alkaline batteries.[37] XG-based hydrogel can be easily obtained at room temperature by dissolving 40.0 mg mL^{-1} in 0.2 mol L^{-1} ferricyanide in 1.0 mol L^{-1} KOH, as depicted in Figure S11b (Supporting Information). The MB exhibited the necessary flexibility and stretchability to conform to body contours without causing discomfort to the user (see Figure 4b; Figure S12a, Supporting Information). Also, it has a comparable size to a coin of quarter-dollar coin (Figure S12a, Supporting Information) and a CR2032 commercial battery (Figure 4b). Figure S12c (Supporting Information) also displays the size measurements of the battery with a digital pachymeter showing the battery is a square-shaped form with 21 mm of side, only 1 millimetre more than the commercial CR2032 assembly. Moreover, the casing size can be easily made even smaller than the one employed on the course of this work since we used a 3D printer to produce the casings molds, which gives us high flexibility in the size and shape of the developed battery while being a very quick procedure.

We employed electrochemical impedance spectroscopy (EIS) to evaluate the conductivity of both the anodic and cathodic hydrogels. The Nyquist plots presented in Figure S13 (Supporting Information) demonstrate the conductivity of BEAQ-gel, ferricyanide-XG-gel, and a 1.0 mol L^{-1} KOH solution, used as a reference. The obtained results show that BEAQ-gel, ferricyanide-XG-gel, and the 1.0 mol L^{-1} KOH solution exhibit conductivities of 0.143 ± 0.015, 0.121 ± 0.015, and 0.106 ± 0.028 S cm^{-1}, respectively, providing strong evidence that both the anodic and cathodic gels possess high conductivities (Equation S6 and Table S6, Supporting Information). The superior conductivity of BEAQ-gel can be attributed to its remarkable self-gelling property, allowing gel formation even at low concentrations, despite being a low-molecular-weight-gelator. Consequently, the abundance of freely available potassium and hydroxide ions at the studied concentration in BEAQ-gel enables their rapid diffusion, leading to a remarkable conductivity. It also suggests the hierarchical 3D structure of BEAQ-gel does not negatively interfere the ionic movement since the conductivities of BEAQ-gel and 1.0 mol L^{-1} KOH solution are not significatively different (Table S6, Supporting Information). This enhanced conductivity further contributes to the improved overall performance of the battery, making BEAQ-gel an excellent choice for enhancing the efficiency of the anode material in the MB configuration. Both BEAQ-gel and Ferricyanide-XG-gel conductivities are similar to or surpass those of some gels utilized in previous energy storage applications (Table S7, Supporting Information).[38,39,40]

Electrochemical characterization was performed by cyclic voltammetry and galvanostatic charging-discharging curves with the battery in flat and bent conformation. The assembled MB has a theoretical capacity and open circuit voltage of 2.4 C and 0.97 V (**Figure 5a**), respectively. Figure 5b–e shows the MB electrochemical performance at 180° bent conformation (Figure S14, Supporting Information). The volumetric capacity was evaluated by charging and discharging the MB at 1.0 and 0.3 V (Figure 5b). After ≈1 h of charging at 1.0 V the battery reached 0.60 mC cm^{-2} μm^{-1} (Figure 5b, black curve), representing a state-of-charge (SOC) of 50%. At the discharging, a volumetric capacity of 0.35 mC cm^{-2} μm^{-1} (0.70 C or) was obtained. It means

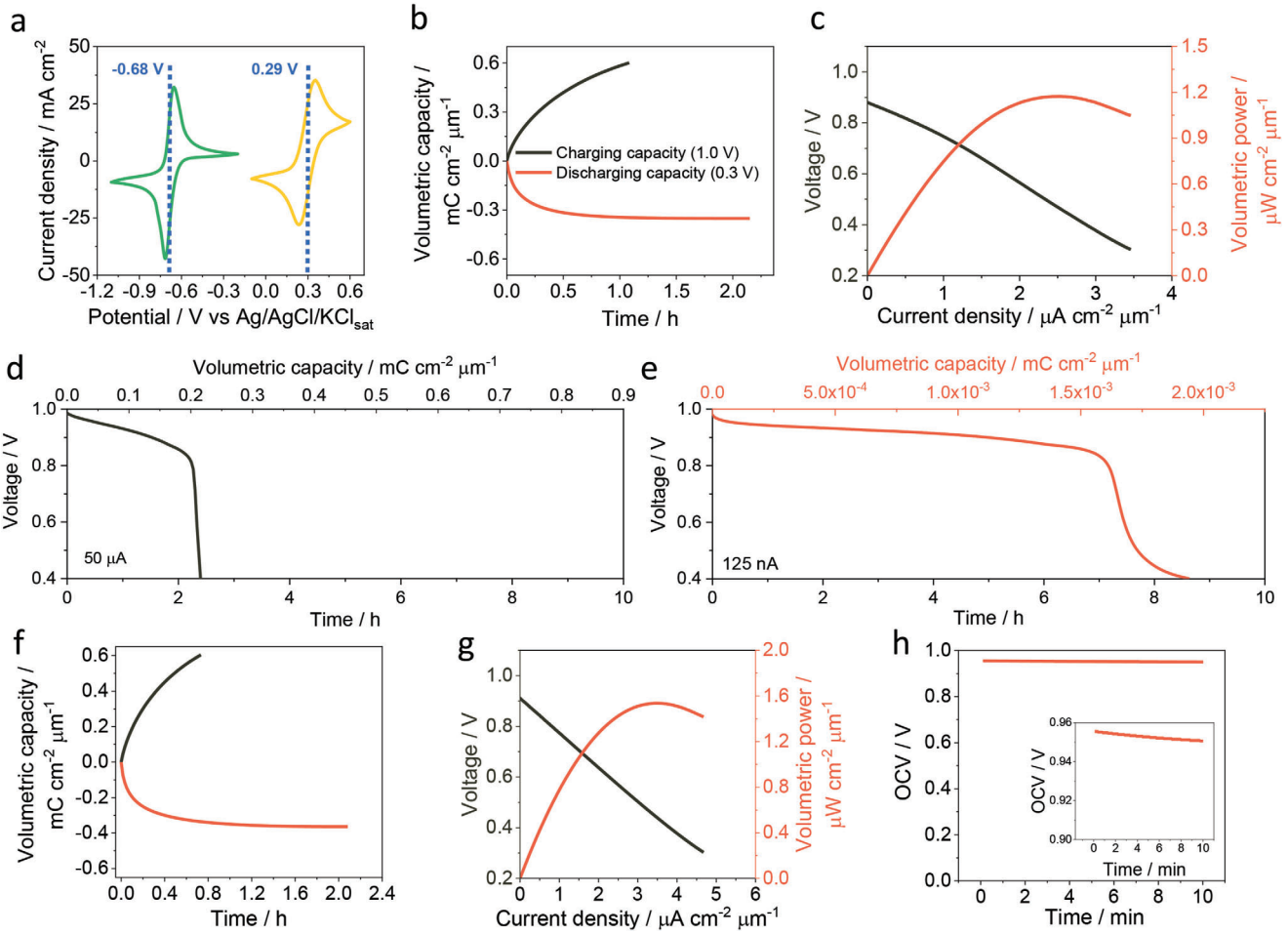

Figure 5. a) CVs of BEAQ-gel (green) and Ferricyanide-XG-gel (yellow) at concentrations equals to 1.5% (w/v) and 0.2 mol L^{-1} of the redox active species, respectively. b) Charging (black) and discharging (red) curves at 1.0 and 0.3 V, respectively. c) Current–voltage (black) and power curve (red), and galvanostatic discharging at d) 50 µA cm^{-2} and e) 125 nA cm^{-2}. All results shown from item b to e were obtained with the wearable battery at 180° bent conformation. f) Charging (black) and discharging (red) curves, g) power (red) and current–voltage (black curves) and h) OCV mesurament during 10 min. The results shown from items f to h were measured using the battery without any bending.

a coulombic efficiency of 59%. The assembled MB exhibits a voltage of 0.89 V, as depicted by the current–voltage (dark-gray) curve in Figure 5c. To the best of our knowledge, this voltage value represents the highest reported voltage for a wearable battery utilizing organic/organometallic active compounds. This is a significative advancement in the development of efficient and high-performance energy storage devices specifically designed for wearable applications.

The maximum volumetric power density (Figure 5c, red line) reached 1.17 µW cm^{-2} $µm^{-1}$ at 2.52 µA cm^{-2} $µm^{-1}$. The galvanostatic discharge curve at 125 nA cm^{-2} (Figure 5e) demonstrates the feasibility of using this MB to power some low consumption wearable devices for 7 h. Using higher current densities, such as 50 µA cm^{-2} (Figure 5d), the battery can also power devices for ≈2.2 h. Some examples of wearable devices this battery could power are presented in **Table 1**.

To assess the impact of the bending process on the electrochemical characteristics of the MB, we performed similar measurements with the wearable MB in a flat conformation (as depicted in Figure 5f–h). The battery in the flat conformation demonstrated an OCV of 0.93 V and a coulombic efficiency of 60%. Moreover, the volumetric power density of the battery in the bent mode was 24% lower than that achieved in the flat mode. However, these differences in the battery's performance in either flat or bent mode attest to its feasibility as a viable power

Table 1. Electrical requirements of some wearable sensors.

Wearable sensor	Power consumption / nW	Voltage / V	Current / µA[a)]	References
Blood pressure	1–5	0.1	50	[41]
	3	0.001	3	[42]
Temperature	75	0.6	0.125	[43]
Tactile pressure	1000	0.1	10	[44]
Ion sensitive Field Effect Transistor	10	0.01[b)]	1	[45]

[a)] The current values were calculated from the power consumption and voltage applied of the sensors; [b)] The voltage considered was the V_{DS} applied in the ISFET.

source for wearable, bendable, and foldable devices. Additionally, we conducted a scaling-up study by producing a battery with a volume four times as large as the miniaturized one. As indicated in Figure S15a,b (Supporting Information), this upscaled battery demonstrated a coulombic efficiency of 62%, a volumetric power density of 0.73 μW cm^{-2} $μm^{-1}$, and a voltage of 0.95 V. These values are comparable to those obtained with the miniaturized batteries in both flat and bent conformations. These results substantiate the potential of the proposed MB to serve as a dependable power source for wearable devices, even when scaled up to larger sizes. A literature survey shows our battery has comparable areal capacity of than other microbatteries, such as zinc[46] and lithium-based microbatteries[47] (Table S8, Supporting Information), which indicates the application of organic molecules to construct micropower energy storage devices is a promising alternative. Furthermore, LMWGs have not been previously applied as active materials for energy storage purposes. Therefore, our work not only contributes to the expansion of knowledge in the field of LMWGs but also proposes a novel application for materials within this class.

3. Conclusion

This work presents the synthesis and a comprehensive characterization of BEAQ-gel, a newly highly conductive material designed for energy storage applications. This new material has important outcomes for the field of energy conversion since open the possibility of developing simple and tunable redox-active gels, which possess application ranging from energy storage to the protection of sensitive (bio) catalysts. Utilizing spectroscopic and scattering techniques, we show 2-BEAQ molecules interact among themselves, with potassium ions and water molecules forming cylindrical aggregates that further entangle forming fibrils and, ultimately, a highly conductive and redox 3D hierarchical network. In addition to its interesting potential as anode, some advantages arise from the use of BEAQ-gel as active material, as its stability over temperatures higher than the human body, its easy synthesis procedure and structure tunability by handling the 2-BEAQ content. Furthermore, by using a low-molecular-weight-gel there is no need of using a thickener agent, which means more volume is available to the active material. The integration of BEAQ-gel with Ferricyanide-XG-gel gave rise to a wearable battery, exhibiting high output voltage and enough volumetric capacity to power low-consumption wearable devices for some hours. This work contributes to advancement in the fundamental understanding of low-molecular-weight gel structure and presents the pioneering application of a redox-responsive, low-molecular-weight gel as a battery anode. This innovation broad the set of an alternative of active materials to produce sustainable and bioinspired wearable batteries in the context of eco-friendly energy solutions. In summary, this pioneer work showcases that organic-based microbatteries are feasible alternatives to power low-consumption energy devices.

4. Experimental Section

See experimental details in the supporting information file provided.

Supporting Information

Supporting Information is available from the Wiley Online Library or from the author.

Acknowledgements

T.B., G.C.S, R.N.P.C., L.J.A.M., and L.C.I.F. acknowledge The São Paulo Research Foundation (FAPESP) by the fellowships with the following numbers 2020/03681-2, 2020/04796-8, 2021/05665-7, 2017/20493-2, and 2019/21089-6, respectively. F.N.C acknowledges FAPESP 2018/22214-6, 2019/15333-1, 2020/12404-2, 2022/09164-5, 2023/01529-7 and Coordination of Superior Level Staff Improvement (CAPES, 23038.003012/2020–16) by the grants. G.B.M.T. acknowledges INCT-FCx (Instituto Nacional de Ciência e Tecnologia de Fluidos Complexos), and CNPq PhD. Scholarship. C.L.P.O. acknowledges FAPESP, Thematic Project; (Grant 2016/24531-3), INCT-FCx, and CNPq Scholarship – Brazil (303001/2019-4). F.C.D.A.L acknowledges FAPESP by the grant 2023/17506-6.

Conflict of Interest

The authors declare no conflict of interest.

Data Availability Statement

The data that support the findings of this study are available from the corresponding author upon reasonable request.

Keywords

anthraquinone, low-molecular-weight-gel, quinone, self-gelling, wearable battery

Received: April 20, 2024
Published online:

[1] J. Shi, S. Liu, L. Zhang, B. Yang, L. Shu, Y. Yang, M. Ren, Y. Wang, J. Chen, W. Chen, Y. Chai, X. Tao, *Adv. Mater.* **2020**, *32*, 1901958.
[2] L. Turini, F. Bonelli, A. Lanatà, V. Vitale, I. Nocera, M. Sgorbini, M. Mele, *Front. Vet. Sci.* **2022**, *9*, 1.
[3] Y. Fang, Y. Zou, J. Xu, G. Chen, Y. Zhou, W. Deng, X. Zhao, M. Roustaei, T. K. Hsiai, J. Chen, *Adv. Mater.* **2021**, *33*, 2104178.
[4] T. Ye, J. Wang, Y. Jiao, L. Li, E. He, L. Wang, Y. Li, Y. Yun, D. Li, J. Lu, H. Chen, Q. Li, F. Li, R. Gao, H. Peng, Y. Zhang, *Adv. Mater.* **2022**, *34*, 2105120.
[5] P. Yang, J. L. Yang, K. Liu, H. J. Fan, *ACS Nano* **2022**, *16*, 15528.
[6] F. N. Crespilho, G. C. Sedenho, D. De Porcellinis, E. Kerr, S. Granados-Focil, R. G. Gordon, M. J. Aziz, *J. Mater. Chem. A* **2019**, *7*, 24784.
[7] T. Bertaglia, L. C. Italiano Faria, J. E. dos Santos Clarindo, F. N. Crespilho, in Advances in Bioelectrochemistry Vol 4 (Ed: F. N. Crespilho), Springer International Publishing, Cham **2022**, pp. 63–87.
[8] M. C. Catoira, L. Fusaro, D. Di Francesco, M. Ramella, F. Boccafoschi, *J. Mater. Sci.: Mater. Med.* **2019**, *30*, 115.
[9] A. Poosapati, S. Vadnala, K. Negrete, Y. Lan, J. Hutchison, M. Zupan, D. Madan, *ACS Appl. Energy Mater.* **2021**, *4*, 4248.
[10] Y. Li, Z. Xu, Y. Liu, S. Jin, E. M. Fell, B. Wang, R. G. Gordon, M. J. Aziz, Z. Yang, T. Xu, *ChemSusChem* **2021**, *14*, 745.
[11] L. Ma, S. Chen, D. Wang, Q. Yang, F. Mo, G. Liang, N. Li, H. Zhang, J. A. Zapien, C. Zhi, *Adv. Energy Mater.* **2019**, *9*, 1803046.

[12] Z. Weng, S. Di, L. Chen, G. Wu, Y. Zhang, C. Jia, N. Zhang, X. Liu, G. Chen, *ACS Appl. Mater. Interfaces* **2022**, *14*, 42494.
[13] A. M. Zamarayeva, A. Jegraj, A. Toor, V. I. Pister, C. Chang, A. Chou, J. W. Evans, A. C. Arias, *Energy Technol.* **2020**, *8*, 1901165.
[14] Y. Wen, F. Li, C. Li, Y. Yin, J. Li, *J. Mater. Chem. B* **2017**, *5*, 961.
[15] Y. Gao, X. Peng, Q. Wu, D. Yang, W. Wang, Q. Peng, T. Wang, J. Wang, J. Liu, H. Zhang, H. Zeng, *ACS Appl. Polym. Mater.* **2022**, *4*, 1836.
[16] Z. Jiang, Y. Li, Y. Shen, J. Yang, Z. Zhang, Y. You, Z. Lv, L. Yao, *Molecules* **2021**, *26*, 2688.
[17] Z. Ji, H. Wang, Z. Chen, P. Wang, J. Liu, J. Wang, M. Hu, J. Fei, N. Nie, Y. Huang, *Energy Storage Mater.* **2020**, *28*, 334.
[18] L. Chen, G. Pont, K. Morris, G. Lotze, A. Squires, L. C. Serpell, D. J. Adams, *Chem. Commun.* **2011**, *47*, 12071.
[19] L. Chen, T. O. McDonald, D. J. Adams, *RSC Adv.* **2013**, *3*, 8714.
[20] P. D. Frischmann, L. C. H. Gerber, S. E. Doris, E. Y. Tsai, F. Y. Fan, X. Qu, A. Jain, K. A. Persson, Y.-M. Chiang, B. A. Helms, *Chem. Mater.* **2015**, *27*, 6765.
[21] Y. Jing, E. M. Fell, M. Wu, S. Jin, Y. Ji, D. A. Pollack, Z. Tang, D. Ding, M. Bahari, M.-A. Goulet, T. Tsukamoto, R. G. Gordon, M. J. Aziz, *ACS Energy Lett.* **2022**, *7*, 226.
[22] D. Wielend, D. H. Apaydin, N. S. Sariciftci, *J. Mater. Chem. A* **2018**, *6*, 15095.
[23] H. Tan, B. Tang, Y. Lu, Q. Ji, L. Lv, H. Duan, N. Li, Y. Wang, S. Feng, Z. Li, C. Wang, F. Hu, Z. Sun, W. Yan, *Nat. Commun.* **2022**, *13*, 2024.
[24] Z. Yoshida, F. Takabayashi, *Tetrahedron* **1968**, *24*, 933.
[25] R. M. Wightman, J. R. Cockrell, R. W. Murray, J. N. Burnett, S. B. Jones, *J. Am. Chem. Soc.* **1976**, *98*, 2562.
[26] A. N Diaz, *J. Photochem. Photobiol., A* **1990**, *53*, 141.
[27] R. H. Peters, H. H. Sumner, *J. Chem. Soc.* **1953**, 2101, https://pubs.rsc.org/en/content/articlelanding/1953/jr/jr9530002101/unauth.
[28] J. Hu, H. Zhang, W. Xu, Z. Yuan, X. Li, *J. Membr. Sci.* **2018**, *566*, 8.
[29] A. Z. Cardoso, L. L. E. Mears, B. N. Cattoz, P. C. Griffiths, R. Schweins, D. J. Adams, *Soft Matter* **2016**, *12*, 3612.
[30] L. Martínez, R. Andrade, E. G. Birgin, J. M. Martínez, *J. Comput. Chem.* **2009**, *30*, 2157.
[31] T. M. Di Palma, F. Migliardini, D. Caputo, P. Corbo, *Carbohydr. Polym.* **2017**, *157*, 122.
[32] P. Shen, Y. Hu, S. Ji, H. Luo, C. Zhai, K. Yang, *Colloids Surf., A* **2022**, *647*, 129195.
[33] D. Jiang, N. Lu, L. Li, H. Zhang, J. Luan, G. Wang, *J. Colloid Interface Sci.* **2022**, *608*, 1619.
[34] C. Yuan, X. Zhong, P. Tian, Z. Wang, G. Gao, L. Duan, C. Wang, F. Shi, *ACS Appl. Energy Mater.* **2022**, *5*, 7530.
[35] W. C. Liu, A. A. R. Watt, *ACS Appl. Nano Mater.* **2021**, *4*, 7905.
[36] N. Luo, W. Dai, C. Li, Z. Zhou, L. Lu, C. C. Y. Poon, S.-C. Chen, Y. Zhang, N. Zhao, *Adv. Funct. Mater.* **2016**, *26*, 1178.
[37] X. Wang, P.-H. P. Wang, Y. Cao, P. P. Mercier, *IEEE Trans. Circuits Syst. I: Regular Papers* **2017**, *64*, 2274.
[38] Z. Zhan, R. Lin, V.-T. Tran, J. An, Y. Wei, H. Du, T. Tran, W. Lu, *ACS Appl. Mater. Interfaces* **2017**, *9*, 37921.
[39] Y. Guo, M. Zhong, Z. Fang, P. Wan, G. Yu, *Nano Lett.* **2019**, *19*, 1143.
[40] C. Yuan, X. Zhong, P. Tian, Z. Wang, G. Gao, L. Duan, C. Wang, F. Shi, ACS Appl Energy Mater **2022**, *5*, 7530.
[41] W. C. Liu, A. A. R. Watt, ACS Appl Nano Mater **2021**, *4*, 7905.
[42] N. Luo, W. Dai, C. Li, Z. Zhou, L. Lu, C. C. Y. Poon, S.-C. Chen, Y. Zhang, N. Zhao, Adv Funct Mater **2016**, *26*, 1178.
[43] X. Wang, P.-H. P. Wang, Y. Cao, P. P. Mercier, IEEE Transactions on Circuits and Systems I: Regular Papers **2017**, *64*, 2274.
[44] Z. Zhan, R. Lin, V.-T. Tran, J. An, Y. Wei, H. Du, T. Tran, W. Lu, ACS Appl Mater Interfaces **2017**, *9*, 37921.
[45] Y. Guo, M. Zhong, Z. Fang, P. Wan, G. Yu, Nano Lett **2019**, *19*, 1143.
[46] Y. Zhou, W. Li, Y. Xie, L. Deng, B. Ke, Y. Jian, S. Cheng, B. Qu, X. Wang, ACS Appl Mater Interfaces **2023**, *15*, 9486.
[47] H. Murata, Y. Nakajima, Y. Kado, N. Saitoh, N. Yoshizawa, T. Suemasu, K. Toko, ACS Appl Energy Mater **2020**, *3*, 8410.

ADVANCED MATERIALS TECHNOLOGIES

Supporting Information

for *Adv. Mater. Technol.*, DOI 10.1002/admt.202400623

Self-Gelling Quinone-Based Wearable Microbattery

*Thiago Bertaglia, Emily F. Kerr, Graziela C. Sedenho, Andrew A. Wong, Rafael N. P. Colombo, Lucyano J. A. Macedo, Rodrigo M. Iost, Luana C. I. Faria, Filipe C. D. A. Lima, Gabriel B. M. Teobaldo, Cristiano L. P. Oliveira, Michael J. Aziz, Roy G. Gordon and Frank N. Crespilho**

Supporting information

Self-gelling Quinone-based Wearable microbattery

Thiago Bertaglia[1], Emily F. Kerr[2, ‡], Graziela C. Sedenho[1,†], Andrew Wong[3,₸], Rafael N. P. Colombo[1], Lucyano J. A. Macedo[1,‖], Rodrigo M. Iost[1], Luana C. I. Faria[1], Filipe C. D. A. Lima[4], Gabriel B. M. Teobaldo[5], Cristiano L. P. Oliveira[5], Michael J. Aziz[3], Roy G. Gordon[2], and Frank N. Crespilho[1,*]

[1]São Carlos Institute of Chemistry, University of São Paulo, São Carlos, SP, Brazil, CEP 13566-590
[2]Department of Chemistry and Chemical Biology, Harvard University, Cambridge, Massachusetts, United States
[3] Harvard John A. Paulson School of Engineering and Applied Sciences, Harvard University, Cambridge, Massachusetts, United States
[4] Federal Institute of Education, Science, and Technology of São Paulo, Campus Matão, São Paulo 15991-502, Brazil
[5] Institute of Physics, University of São Paulo, São Paulo, SP, Brazil, CEP 05508-090

Current addresses

‡ Xavier University Chemistry Department, 3800 Victory Pkwy, Cincinnati, OH 45207
† Department of Chemistry, Federal University of São Carlos, Rod. Washington Luís, s/n, São Carlos, SP, 13565-905, Brazil.
₸ Livermore National Laboratory, Livermore, California, United States
‖Brazilian Synchrotron Light Laboratory, Brazilian Center for Research in Energy and Materials, Rua Giuseppe Máximo Scolfaro, 10.000, Campinas, Sao Paulo, 13083-970, Brazil

*E-mail address: frankcrespilho@usp.br (F.N.Crespilho)

Table of Contents

1. Experimental section

1.1. Materials and reagents

Hydrochloric acid, potassium ferricyanide, xanthan gum, and Nafion® 212 membrane were purchased from Sigma-Aldrich®. Potassium hydroxide, sulfuric acid, and potassium permanganate were acquired from Synth®. The flexible carbon fiber (FCF), called HPCCE-5H, was obtained from Delpho Instruments. BEAQ was synthesized according to the methods in section 1.3. All experiments were carried out using ultrapure water from a Direct-Q®3 water purification system with a resistance of 18.2 MΩ×cm.

1.2. FCF-based electrode production

The FCF electrodes were chemically treated as previously reported.[1] Briefly, 0.5 g of FCF were extracted, immerse in 120 mL of a 20.0 mmol L^{-1} $KMnO_4$ in 1.0 mol L^{-1} H_2SO_4, and kept under sonication for 3 h. Then, FCF was washed with concentrated hydrochloric acid and water and dried under vacuum overnight. To produce the electrodes, one FCF array was extracted from the treated cloth and had its geometrical area limited with paraffin. After paraffin curing, it was employed as working electrode in the electrochemical measurements.

1.3. BEAQ synthesis procedure

1 gram of 2-hydroxyanthraquinone (4.45 mmol) was mixed with 1.5 g potassium carbonate (10.9 mmol, 2.45 eq) in 4 mL of anhydrous dimethylformamide and 1.5 mL of ethyl 4-bromobutyrate (2.04 g, 10.4 mmol, 2.35 eq). The mixture was stirred at 85 ^{o}C for 80 minutes during which time a sandy solid precipitated out. 5 mL of water was added to the solution followed by vacuum filtration. The solid was added without purification to a flask containing 4.5 g potassium hydroxide (80.3 mmol, 18 eq), 45 mL of water, and 45 mL of 2-propanol and stirred at 85 ^{o}C for three hours, resulting in a dark solution. Glacial acetic acid was then added until the solution formed a green precipitate which was vacuum filtered. 0.83 g of a yellow-green solid was obtained (63% yield). H^1

NMR: 8.19 (3H, m), 7.92 (2H, quint), (7.60, 1H, d), 7.45 (1H, dd), 4.24 (2H, t), 2.24 (2H, t), 2.01 (2H, quint). Unintegrated peaks belong to DMSO-d5 and water.

1.4. Cyclic voltammetry of BEAQ, BEAQ-gel, and ferricyanide-XG-gel

Electrochemical measurements were carried out in a PGSTAT128N (Autolab®, Metrohm) coupled with a three-electrode electrochemical cell and FCF-based, platinum, and Ag/AgCl/KCl_{sat} as working, auxiliary, and reference electrodes, respectively. The cyclic voltammograms were recorded using 1 $mmol^{-1}$ BEAQ in 1 M KOH, BEAQ-gel (1.50 % (w/v) BEAQ in 1.0 mol L^{-1} KOH) or ferricyanide-XG-gel (0.2 mol L^{-1} $K_4[Fe(CN)_6]$ in 1.0 mol L^{-1} KOH and 40 mg mL^{-1} Xanthan gum) as electrolyte, at 5, 25, 50, 75 and 100 mV s^{-1}. The potential was swept from -1.0 and -0.2 V for BEAQ and BEAQ-gel and from 0.0 to 0.6 V for ferricyanide-XG-gel. The measurement in solution was carried out in a degassed electrolyte and argon atmosphere and those with BEAQ-gel and ferricyanide-XG-gel with ohmic drop correction available in NOVA 2.1.5 software.

1.5. Linear sweep voltammetry coupled with rotating disk electrode

Rotating disk electrode (RDE) measurements were performed in a modulated speed rotator from Pine Research® (Model AFMSRCE) employing a glassy carbon disk (GC), a platinum plate, and Ag/AgCl/KCl_{sat} as working, auxiliary, and reference electrodes, respectively. Before each measurement, GC was polished with alumina 0.05 μm, rinsed with ultrapure water, and sonicated in ultrapure water for 10 min. The linear sweep voltammograms were performed from -0.2 V to -1.0 V at 10 mV s^{-1} in 1.0 mmol L^{-1} BEAQ in 1.0 mol L^{-1} KOH solution at 100, 200, 300, 400, 500, 700, 900, 1200, 1600, 2000, 2500, and 3000 rpm.

Levich formalism (Equation S1) correlates the steady-state current of a given electrochemical reaction under convective mass transport with the square root of the rotation rate of the electrode and allows us to calculate the diffusion coefficient of the reactant. In equation S1, J_{ss} is the steady-state current density, n the number of electrons, F is the Faraday constant, A is the electrode area, ω the rotation rate, D is the diffusion coefficient, v is the kinematic viscosity of the solution, and C is the concentration of the reactant. The plot I vs $\omega^{1/2}$ gives a

straight line with slope proportional to the diffusion coefficient of the studied compound as we can see in equation S2.

$$J_{ss} = (0.620)nFD^{2/3}\omega^{1/2}\nu^{-1/6}C \quad \text{Equation S1}$$

$$Slope\left(J_{ss}\ vs\ \omega^{\frac{1}{2}}\right) = (0.620)nFD^{2/3}\upsilon^{-1/6}C \quad \text{Equation S2}$$

1.6. Pourbaix diagram

The Pourbaix diagram shows a plot of half-wave potential ($E_{1/2}$) versus *pH* and gives information about the number of protons and electrons involved in the electrochemical reaction in a defined solution pH. Cyclic voltammetry (CV) measurements from -1.00V to -0.2 V at 5 mV s^{-1} and argon atmosphere were performed in 1.0 mmol L^{-1} BEAQ solutions prepared in 0.1 mol L^{-1} Britton-Robinson buffer with pH values ranging from 8.0 to 12.0 and in 0.1 mol L^{-1} and 1.0 mol L^{-1} KOH solutions at pHs values equal to 13.0 and 14.0, respectively. The $E_{1/2}$ values in each pH conditions were obtained and we processed the obtained results according to Equation S3 and S4, which shows the Nernst equation modified to consider the solution pH and their first derivative, respectively. The slope of the obtained curves indicated the number of electrons (*n*) and protons (*m*) that participates of the electrochemical reactions. In equations S3, *E*, E^0 and $[H^+]$ have their common meanings.[2,3]

$$E = E^0 - \frac{0.05916}{n}\log\frac{1}{[H^+]^m} \quad \text{Equation S3}$$

$$\frac{\partial E}{\partial pH} = 0.05916\frac{m}{n} \quad \text{Equation S4}$$

1.7. UV-Vis spectroscopy and UV-Vis spectroelectrochemistry

UV-Vis spectra were recorded in a JASCO V-670 equipped with previously cleaned quartz cuvettes and sweeping the radiation wavelength from 800 to 190 nm. The spectroelectrochemical measurements were carried out using a

homemade FCF-based optically transparent thin-layer electrode, a platinum wire and Ag/AgCl/KCl_{sat}, as working, auxiliary, and reference electrodes, respectively. The potential was swept from -0.90 to -0.30 V with steps of 0.10 or 0.05 V using a PGSTAT204 (Autolab, Metrohm) and all spectra were recorded after 15 min of potential application. We fitted the obtained results with the Nernst equation (Equation S5) and obtained *n* and $E^{0'}$ for both oxidation (-0.90 to -0.30 V) and reduction (-0.20 to -0.90 V) measurements. The fit used *T* as 298 K, R as 8.314 J K^{-1} mol^{-1} and F as 96485 C mol^{-1}.

$$I_{Total} = \left(\frac{I_{max}^{1}}{\left\{ 1 + e^{\left[(E - E_1^0) \times \frac{nF}{RT} \right]} \right\}} \right) \qquad \text{Equation S5}$$

1.8. Rheology measurements

The BEAQ-gel rheological properties were measured in a Discovery HR-3 Rheometer (TA Instruments, USA) equipped with 40 mm stainless steel parallel Peltier plates and 500 µm of plate gap. The temperature sweep was performed from 25 to 45 °C with increments of 5 °C and 10 rad s^{-1} as angular frequency. The amplitude sweeps used an angular frequency of 10 rad s^{-1} from 1 × 10^{-5} to 5 × 10^{-2} rad at 25 °C to 45 °C and the frequency sweeps from 0.1 to 100.0 rad s^{-1} with 2.5 × 10^{-4} rad displacement and between 25 °C to 45 °C.

1.9. FTIR and Raman of BEAQ powder, K-BEAQ, and D_2O-K-BEAQ-gel

The FTIR spectra of BEAQ powder, K-BEAQ, and D_2O-K-BEAQ-gel were acquired from 4000 to 600 cm^{-1} in a Vertex 70v infrared spectrometer (Bruker) equipped with the platinum attenuated total reflectance (ATR) module (diamond crystal) and liquid nitrogen-cooled mercury-cadmium-telluride (MCT) detector. All spectra are the average of 48 scans with resolution of 4 cm^{-1} and were recorded in evacuated environment. K-BEAQ sample was produced by freeze-drying the 1.5% (w/v) BEAQ in 1.0 mol L^{-1} KOH solution and D_2O-K-BEAQ gel comprised of

the gel produced from dissolution of 1.5% (w/v) in 1.0 mol L^{-1} KOH solution produced in deuterium dioxide.

Raman spectra were obtained on LabRam HR Evolution equipped with a 1600 × 200 CCD detector (symphony; thermoelectric cooled), an 1800 L mm^{-1} grating, a HeNe laser with an excitation wavelength of 633 nm (red laser), filter 10%, a 100× objective, and a detection pinhole of 100 mm. The spectrometer was calibrated by determining the wavenumber position of Raman line of a silicon substrate at 520.7 cm^{-1} before data acquisition. Briefly, the samples were positioned onto a borosilicate slide and mapped until reaching the desired region, where the Raman spectra were recorded.

1.10. Synthesis of BEAQ-gel and Ferricyanide-XG-gel

BEAQ-gel was synthesized by simple solubilization of 1.55 mg of BEAQ in 100 µL of 1.0 mol L^{-1} KOH under sonication until no vestiges of solid BEAQ or aggregated could be observed. For ferricyanide-XG-gel synthesis, 4 mg of xanthan gum polymer were added to 100 µL of 0.2 mol L^{-1} of $K_4[Fe(CN)_6]$ in 1.0 mol L^{-1} KOH and then vortexed by 10 min or until an homogeneous light-yellow gel could be observed.

1.11. Conductivity measurements of BEAQ-gel, ferricyanide-XG-gel, and KOH

To calculate the conductivity of 1.0 mol L^{-1} KOH solution, BEAQ-gel and ferricyanide-XG-gel we developed a square-shaped 3D printed electrochemical cell, where two FCF arrays were glued and served as electrodes to electrochemical impedance spectroscopy (EIS) measurements. EIS spectra were recorded from 0.1 to 10^5 Hz at the open circuit potential of each sample using 10 mV as potential amplitude. The samples were kept in nitrogen atmosphere to avoid any interference of oxygen. We calculated the conductivity Equation S6, where *L* is the thickness of the sample, *A* is the electrode area, and *R* is the sample resistance. *R*-values were obtained from the x-intercept of Nyquist plots.

$$\kappa = \frac{L}{A \times R}$$ Equation S6

1.12. Small-angle X-ray Scattering measurements and processing

Small-angle X-ray scattering (SAXS) data were acquired in a modified NanoStar (Bruker) equipment with Xenocs source, focusing mirror and collimation system. The source is a microfocus GeniX3D system with Cu Kα tube (λ=1.54Å). The beam is focused by Fox3D mirrors and the collimation is performed by two sets of scatterless slits. As a result a beam with 1x1mm^2 is obtained and the experiments are performed in transmission mode. The 2D scattering data is collected on a Dectris-Pilatus 300K detector placed at 630mm from the sample position. The detector is integrated in the same vacuum path, without windows or beam stopper, which decreases the experimental parasitic background. The 2D scattering images are azimuthally integrated by the program Fit2D.[4] As a result one obtains 1D curves of the Intensity as a function of the modulus of the reciprocal space vector q, defined as $q=4\pi sen(\theta)/\lambda$, where 2θ is the scattering angle. The normalization factor for each sample is obtained from the forward beam (central part of the 2D image). Prior the measurements the 0.07%, 1.50%, 3.00%, and 4.5% (w/v) BEAQ-gel samples were heated at 50°C until become fluid and inserted in disposable glass capillaries with diameter of 1.5 mm. Following, the capillaries were sealed with vacuum resistant commercial resin and the scattering data acquired by exposing each sample to 1800 seconds in vacuum environment and room temperature. Silver behenate was employed as standard for distance calibration. All scattering data are the average of four different measurements.

We processed the SAXS data using SuperSAXS home-made software[5] by subtracting the scattering of the solvent (1 mol L^{-1} KOH) from each sample. To gather information about the supramolecular structures we fitted the data according to a diffuse cylinder model, as shown in equation S7.

$$I(q) = Sc_1 P_c(q, R_c, \sigma_c, \sigma_{int})\, P_{rod}(q, L)\, S_{cyl}(q, \nu)$$ Equation S7

In this expression the decoupling approximation[6] is used for the contributions of the cylinder length and cross section. $P_{rod}(q)$ accounts for an infinitely thin rod with length L.[7] $P_c(q)$ accounts for the intensity of a circle with radius R_c,

polydispersity σ_c and smeared outer interface (Gaussian) with σ_{int}. Long cylinders can show structure factor effects, which can be described by the factor $S_{cyl}(q)$ assuming the Random Phase Approximation (RPA)[8] with the interaction factor ν. A Hankel transformation of the radial scattering amplitude $F_c(q)$ ($P_c(q) =< F_c(q) >^2$) provides the radial electron density profile of the cylinders. Mathematical details about the model are available in reference [9].

1.13. Wearable battery assembly and electrochemical characterization

Prior to assembly the battery, we developed a square-shaped flexible by allowing silicon acetic resin to cure in a previously 3D printed mold (see Figure 4b in the manuscript). To accommodate BEAQ-gel and Ferricyanide-XG-gel we designed a square-shaped hole inside the flexible casing with dimensions of 1.0 × 1.0 × 0.2 cm. All recorded battery data were normalized by 2,000 cm^2 μm^1, which is the volume of the square-shaped hole at the given units. A larger casing with dimensions of 2.0 × 2.0 × 0.2 cm was also fabricated and 8,000 cm^2 μm^1 was employed as normalization constant in the data processing for those batteries. The black color was to mitigate the influence of environment in the battery during the electrochemical measurements.

We assembled the wearable battery by transferring 250 µL (or 1 mL) of BEAQ and 250 µL (or 1 mL) of Ferricyanide-XG-gel for two different casing pieces. Then, at the top of each chamber we added a previously cut 1.0 cm^2 FCF-based current collector wired with a FCF, used as electrical contact external to the battery. Finally, the battery was closed with silicon acetic resin. The assembled battery rested overnight (around 18 h) aiming the silicon acetic to cure and the hydration of the membrane by the hydrogels inside the battery. The battery electrochemical characterization occurred by charging it at 1.00 V until to reach a state-of-charge (SOC) of 50% and sequentially discharging at 0.30 V. The current-voltage and power curves for the battery at SOC of 50% were obtained by cyclic voltammetry at 100 mV s^{-1}. All measurements were performed with the battery in flat and 180° bent conformation in nitrogen atmosphere. The galvanostatic discharge curve was obtained by draining 50 µA cm^{-2} and 125 nA cm^{-2} of the battery until it reaches 0.4 V. The assembled battery has theoretical capacity and voltage of 2.4 C (or 9.6 C) and 0.97 V, respectively.

2. ^{1}H NMR

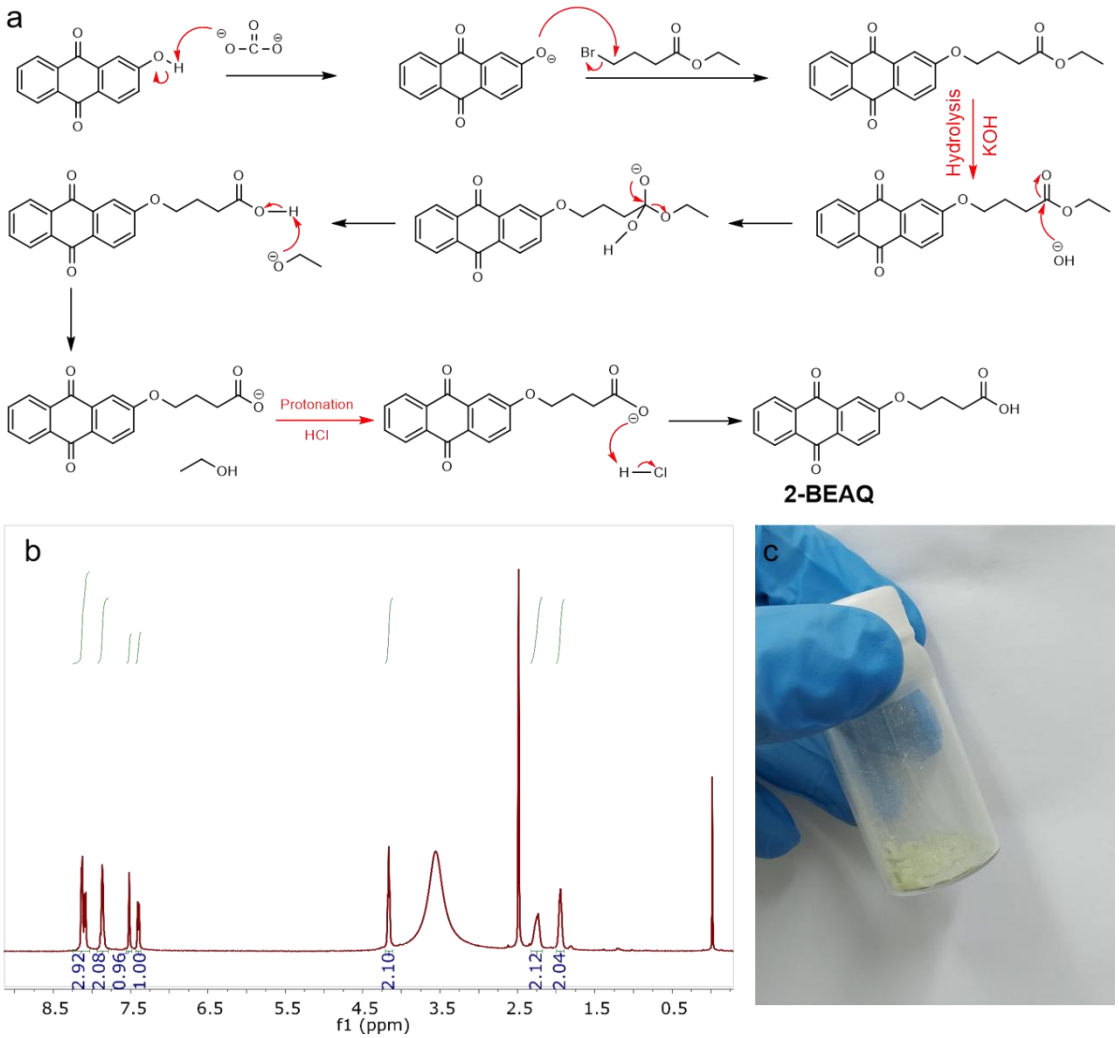

Figure S1. (a) Reaction mechanism for synthesizing 2-BEAQ using 2-hydroxianthraquinone as precursor**,** (b) ^{1}H NMR spectrum of 2-BEAQ in DMSO-*d6* and (c) photograph of 2-BEAQ at room temperature.

2-BEAQ synthesis took place by deprotonating the side chain of 2-hydroxyanthraquinone followed by a nucleophilic substitution on 4-ethylbromobutyrate. Then, the produced ester was hydrolyzed in alkaline media and the solution acidified with concentrated hydrochloric acid, giving rise 2-BEAQ as a light-green precipitate. A detailed description of the reaction mechanism and a photograph of the obtained powder are shown in Figure S1a and b. Figure S1c exhibits the ^{1}H NMR of 2-BEAQ. The region between 8.5 to 7.0 ppm is integrated to seven hydrogen atoms and represents all the hydrogen atoms attached to the anthraquinone core. Furthermore, the region between 4.5 to 1.5 ppm presents five more signals, three related to the molecule and two related to the solvent

used in the analysis. The signal at 4.16 ppm is a triplet integrated for two hydrogen atoms and is assigned to the C1 of the 2-BEAQ's butyl side chain. This signal is a triplet since the hydrogen atoms in C1 couples with that in C2. Also, it appears in a less shielded spectral region since the ether group has high electronegativity and deshields both C1 and the hydrogen atoms attached into it. The signal at 2.23 ppm is also triplet and is assigned to the hydrogen in C3 of 2-BEAQ's butyl side chain. It appears also as triplet since the hydrogens in C3 couples with that in C2. Finally, the signal at 1.94 ppm is assigned to the hydrogens in C2 of the BEAQ's butyl side chain and is a multiplet as these hydrogens couples with that in C1 and C3. Also, it appears at a more shielded region since it is not bonded to any other more electronegative atom and the effect of both ether and carboxylic acid moieties have almost no influence on this chemical environment.

3. Data extracted from the CV of 1.0 mmol L^{-1} BEAQ in 1.0 mol L^{-1} KOH

Table S1. Cathodic and anodic peak potentials and current densities, peak separation, half-wave potential and j_{pa} / j_{pc} ratio for 1.0 mmol L^{-1} BEAQ in 1.0 mol L^{-1} KOH.

Scan rate/ mV s^{-1}	E_{pa}/ V	E_{pc}/ V	ΔE_p/ V	$E_{1/2}$/ V	j_{pa}/mA cm^{-2}	j_{pc}/ mA cm^{-2}	j_{pa}/j_{pc}
5	-0.650 ± 0.005	-0.685 ± 0.003	0.035 ± 0.008	-0.668 ± 0.002	2.206 ± 1.125	-2.311 ± 1.142	0.949 ± 0.022
25	-0.642 ± 0.008	-0.693 ± 0.008	0.051 ± 0.016	-0.668 ± 0.001	6.808 ± 2.450	-7.251 ± 2.856	0.950 ± 0.043
50	-0.634 ± 0.012	-0.700 ± 0.009	0.065 ± 0.021	-0.667 ± 0.002	10.944 ± 3.446	-11.443 ± 3.941	0.965 ± 0.038
75	-0.629 ± 0.013	-0.706 ± 0.010	0.077 ± 0.023	-0.668 ± 0.002	13.723 ± 3.819	-14.263 ± 4.417	0.971 ± 0.044
100	-0.625 ± 0.014	-0.711 ± 0.013	0.086 ± 0.027	-0.668 ± 0.001	16.345 ± 4.266	-16.843 ± 5.055	0.981 ± 0.053

4. Calculation of BEAQ's diffusion coefficient

Figure S2a,b shows the linear sweep voltammograms and Levich plot obtained for 1 mmol L^{-1} BEAQ in 1 mol L^{-1} KOH solution. The Levich plot (**Figure S2b**) shows a straight line with equation y = 0.026 + 0.054x with R^2 equals to 0.99992. Equation S2 was mathematically rearranged to express BEAQ diffusion coefficient (*D*) value and then we substituted *n* as 2, *v* as 0.01 cm s^{-1}, *C* as 1.0 mmol L^{-1}, F as 96485 C mol^{-1}, and slope (J_{ss} vs $\omega^{1/2}$) as 0.054. All calculation steps follow below.

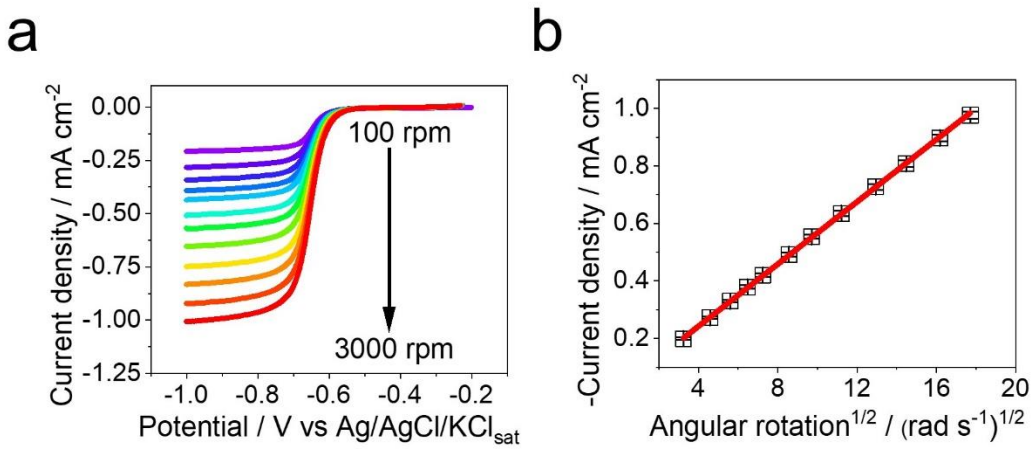

Figure S2. (a) Linear sweep voltammograms recorded with 1.0 mmol L^{-1} BEAQ in 1.0 mol L^{-1} KOH using glassy carbon rotating disk electrode at 100, 200, 300, 500, 700, 900, 1200, 1500, 2000, 2500, and 3000 rpm. (b) Levich plot built up with stedy-state currents from the linear sweep voltammograms.

$$Slope\left(J_{ss}\ vs\ \omega^{\frac{1}{2}}\right) = (0.620)nFD^{2/3}\upsilon^{-1/6}C$$

$$D = \left(\frac{Slope\left(J_{ss}\ vs\ \omega^{\frac{1}{2}}\right)}{n \times F \times \upsilon^{-1/6} \times C \times 0.620}\right)^{3/2}$$

$$D = \left(\frac{0.054}{2 \times 96485 \times 0.01^{-1/6} \times 1 \times 10^{-3} \times 0.620}\right)^{3/2}$$

$$D = \left(\frac{0.054}{257.76}\right)^{3/2} = 3.04 \times 10^{-6}\ cm^2 s^{-1}$$

5. Diffusion coefficient and half-wave potential values for some organic/organometallic compounds reported in energy storage application.

Table S2. Values of diffusion coefficient and electrochemical reaction potential of some organic molecules employed in energy storage devices.

Compound	Diffusion Coefficient ($cm^2\ s^{-1}$)	Half-wave potential (V vs SHE)	References
BTMAP-Vi	3.3×10^{-6}	-0.36	[10]
2,6-DPPEAQ	1.37×10^{-6}	-0.47	[11]
2,6-DHAQ	4.8×10^{-6}	----	[12]
BPP-Vi	$2.7 / 2.6 \times 10^{-6}$ *	-0.46	[13]
DPivOHAQ	2.4×10^{-6}	-0.48	[14]
DBAQ	2.5×10^{-6}	-0.47	[14]
AQDP	9.7×10^{-7}	-0.456	[15]
BEAQ	3.04×10^{-6}	-0.46	This work

BTMAP-Vi: bis(3-trimethylammonio)propyl viologen tetrachloride; **2,6-DPPEAQ:** (((9,10-dioxo-9,10-dihydroanthracene-2,6-diyl)bis(oxy))bis(propane-3,1-diyl))bis(phosphonic acid); **2,6-DHAQ**: 2,6-dihydroxyanthraquinone; **BPP-Vi**: 1,1′-bis(3-phosphonopropyl)-[4,4′-bipyridine]-1,1′-diium dibromide; **DPiVOHAQ:** 3,3′-(9,10-anthraquinone-diyl)bis(3-methylbutanoic acid; **DBAQ:** 4,4′-(9,10-anthraquinone-diyl)dibutanoic acid; **AQDP:** 9,10-anthraquinone-2,6-dipropionic acid
*Oxidized and reduced forms, respectively.

6. BEAQ mechanism reaction according to the solution pH

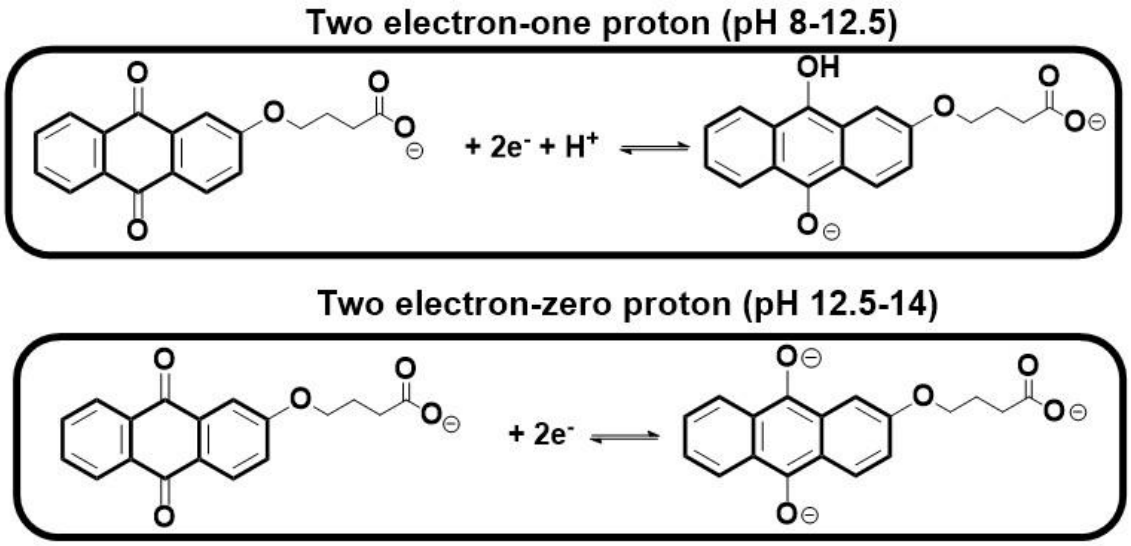

Figure S3. Illustration of the electrochemical reaction mechanism of BEAQ according to the solution pH.

7. UV-vis spectra of oxidized BEAQ

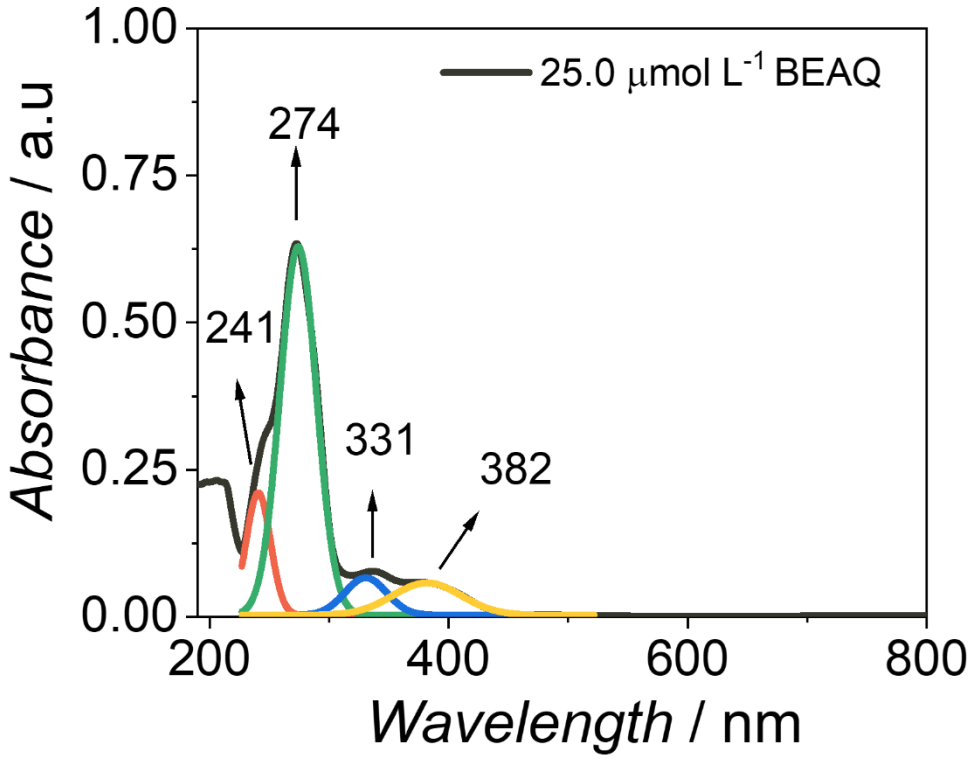

Figure S4. UV-vis spectrum of 25.0 μmol L^{-1} BEAQ in 1.0 mol L^{-1} KOH. The red, green, blue, and yellow curves show the peak fitting of the spectra.

8. Images of BEAQ-gel at different concentrations

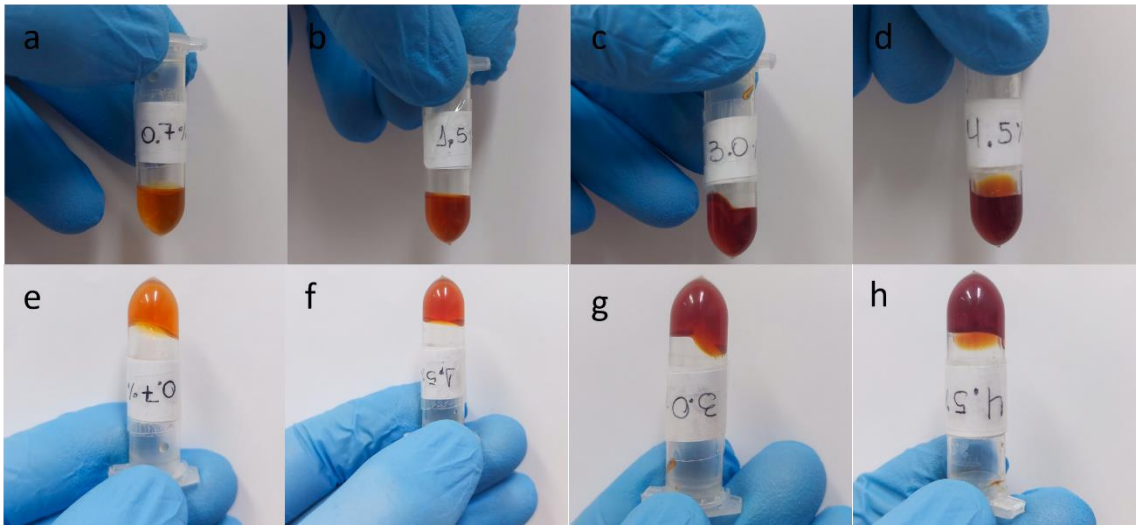

Figure S5. Images of BEAQ-gel at different concentrations and their respective upside-down gelation test. (a) and (e) show images at 0.7%, (b) and (f) show images at 1.5%, (c) and (g) show images at 3.0%, and (d) and (h) show images at 4.5%.

9. Images of BEAQ-gel and BEAQ suspension in 1.0 mol L^{-1} NaOH

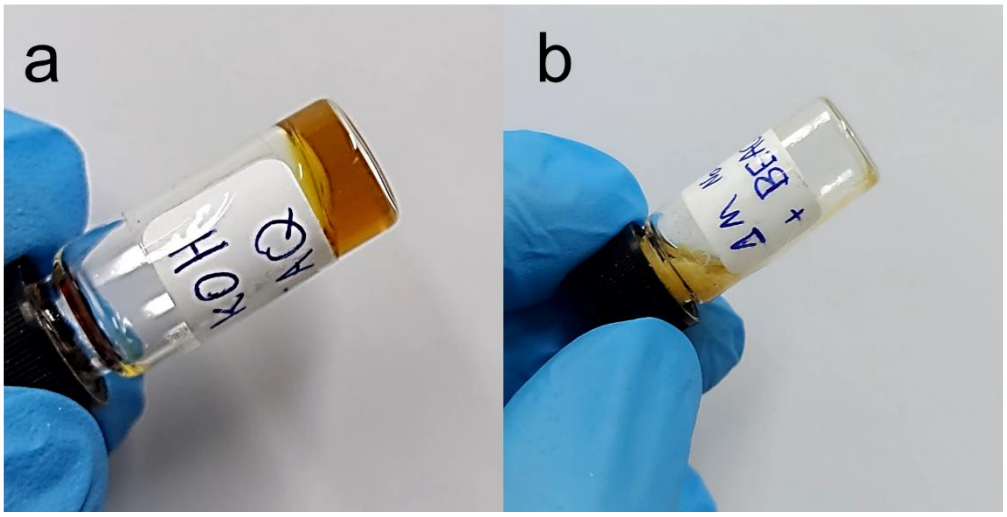

Figure S6. Images of the hydrogel and suspension obtained from the dissolution of 1.50% (w/v) BEAQ in (a) 1.0 mol L^{-1} KOH (BEAQ-gel) and in (b) 1.0 mol L^{-1} NaOH. The pH values of KOH and NaOH solution are 13.7 and 13.4, respectively.

10. Data extracted from the CV recorded in BEAQ-gel (1.5% (w/v) BEAQ in 1.0 mol L^{-1} KOH)

Table S3. Cathodic and anodic peak potentials and current densities, peak separation, half-wave potential and j_{pa} / j_{pc} ratio for cyclic voltammograms of BEA-gel.

Scan rate/ mV s^{-1}	E_{pa}/ V	E_{pc}/ V	ΔE_p/ V	$E_{1/2}$/ V	j_{pa}/mA cm^{-2}	j_{pc}/ mA cm^{-2}	j_{pa}/j_{pc}
5	-0.660 ± 0.012	-0.708 ± 0.044	0.049 ± 0.026	-0.684 ± 0.001	0.024 ± 0.011	-0.030 ± 0.012	0.816 ± 0.057
25	-0.633 ± 0.027	-0.738 ± 0.047	0.104 ± 0.069	-0.686 ± 0.008	0.100 ± 0.027	-0.112 ± 0.032	0.894 ± 0.017
50	-0.613 ± 0.046	-0.757 ± 0.056	0.144 ± 0.103	-0.685 ± 0.006	0.160 ± 0.041	-0.174 ± 0.040	0.917 ± 0.030
75	-0.602 ± 0.054	-0.772 ± 0,062	0.170 ± 0.121	-0.687 ± 0.006	0.213 ± 0.047	-0.223 ± 0.040	0.950 ± 0.052
100	-0.589 ± 0.054	-0.782 ±0,062	0.193 ± 0.124	-0.685 ± 0.009	0.266 ± 0.048	-0.273 ± 0.025	0.970 ± 0.092

11. Dependence of loss and storage moduli of BEAQ gel with oscillation stress

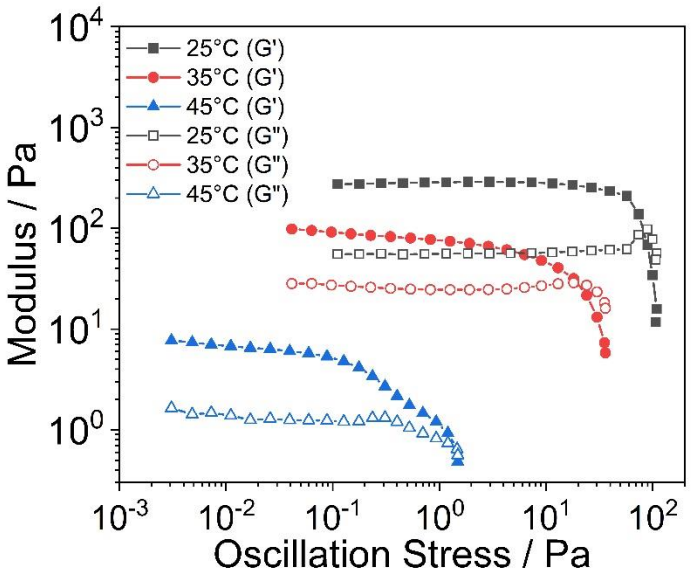

Figure S7. Dependence of storage and loss moduli with the oscillation stress for 0.1 mol L^{-1} BEAQ in 1.0 mol L^{-1}.

12. Assignments of BEAQ powder FTIR absorptions

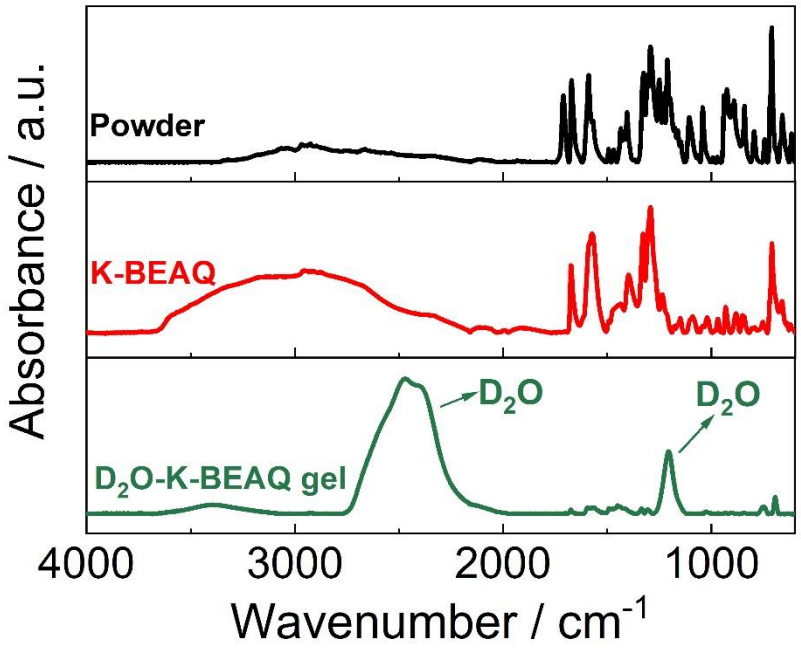

Figure S8. FTIR spectra of BEAQ powder, K-BEAQ and, D_2O-K-BEAQ-gel.

Table S4. Infrared absorption signals of BEAQ powder and their respective assignments.[16]

Wavenumber / cm^{-1}	Assignment
2926	vO-H / vC-H
1711	vC=O
1670	vC=O
1589	vC=C
1572	v_{ass}C=O
1404	v_sC=O
1292	vC-O
1250	v_sC-O-C
1042	v_{ass}C-O-C
925	δC=C
710	δC-H

13. BEAQ-gel stoichiometry calculation

The 1.50% (w/v) BEAQ-gel stoichiometry was calculated based on the concentrations of each hydrogel constituent. For this, we employed 50 mmol L^{-1}, 1 mol L^{-1}, and 55.5 mol L^{-1} for BEAQ-COO^-, KOH, and H_2O concentrations. FTIR results shows that all BEAQ molecules are deprotonated at the studied pH, thus we subtracted 50 mmol L^{-1} from the hydroxide initial concentration. The 1.50% (w/v) BEAQ-gel stoichiometry is 1110: 20: 19: 1 considering H_2O/ K^+/ OH^-/ BEAQ-COO^- as shown below.

$$\frac{H_2O}{BEAQ - COO^-} = \frac{55.5\ mol\ L^{-1}}{50.0\ mmol\ L^{-1}} = 1110$$

$$\frac{K^+}{BEAQ - COO^-} = \frac{1.0\ mol\ L^{-1}}{0.05\ mmol\ L^{-1}} = 20$$

$$\frac{OH^-}{BEAQ - COO^-} = \frac{0.95\ mol\ L^{-1}}{50.0\ mmol\ L^{-1}} = 19$$

Two different sets of simulations were performed using Packmol software. The first one (**Figure 3g**) simulated the structure of BEAQ gel in the previously calculated stoichiometry by using a cube with 71 Å as edge size and 11,100/ 200/ 190/10 as total number of H_2O, K^+, OH^-, and BEAQ-COO^-.[17] This simulation presents random distribution of K^+, BEAQ-COO^-, OH^-, and H_2O over the whole box. The second simulation (**Figure 4h-j**) was performed to visualize the cylinder formation by BEAQ-COO^-, the key supramolecular structure, which enables the gelation process to occur. A total number of 15,000 /1,000 /950/ 50 (H_2O/ K^+/ OH^- / BEAQ-COO^-) were employed. It is important to note we chose a lower amount of water molecules to better observe the cylindrical supramolecular structure. The obtained data were processed using PyMol and H_2O, K^+ and OH^- were made transparent when convenient to improve the visualization of BEAQ-COO^- molecules. Atomic color representation: carbon (green), oxygen (red), hydrogen (white), and potassium (purple).

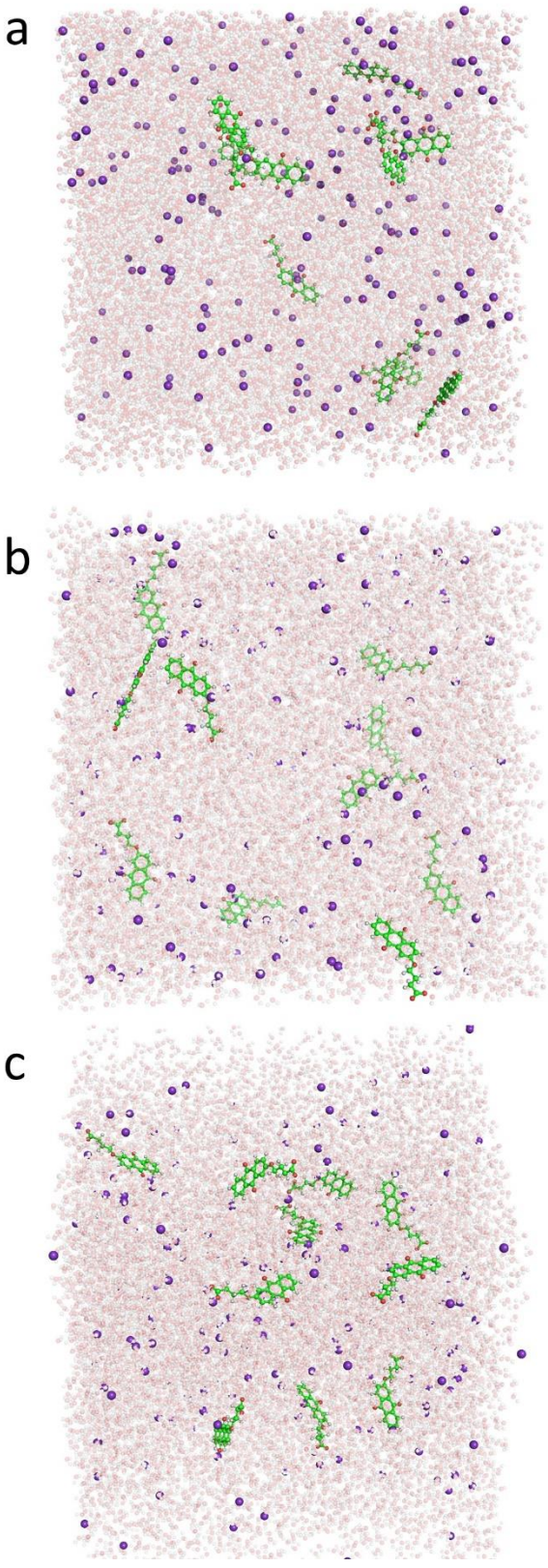

Figure S9. Arrangement of BEAQ-COO^- molecules in a cube with 71 Å of edge size. The three different cubes represent three independent arrangements designs. The number of BEAQ-COO^- molecules is 10.

14. SAXS data

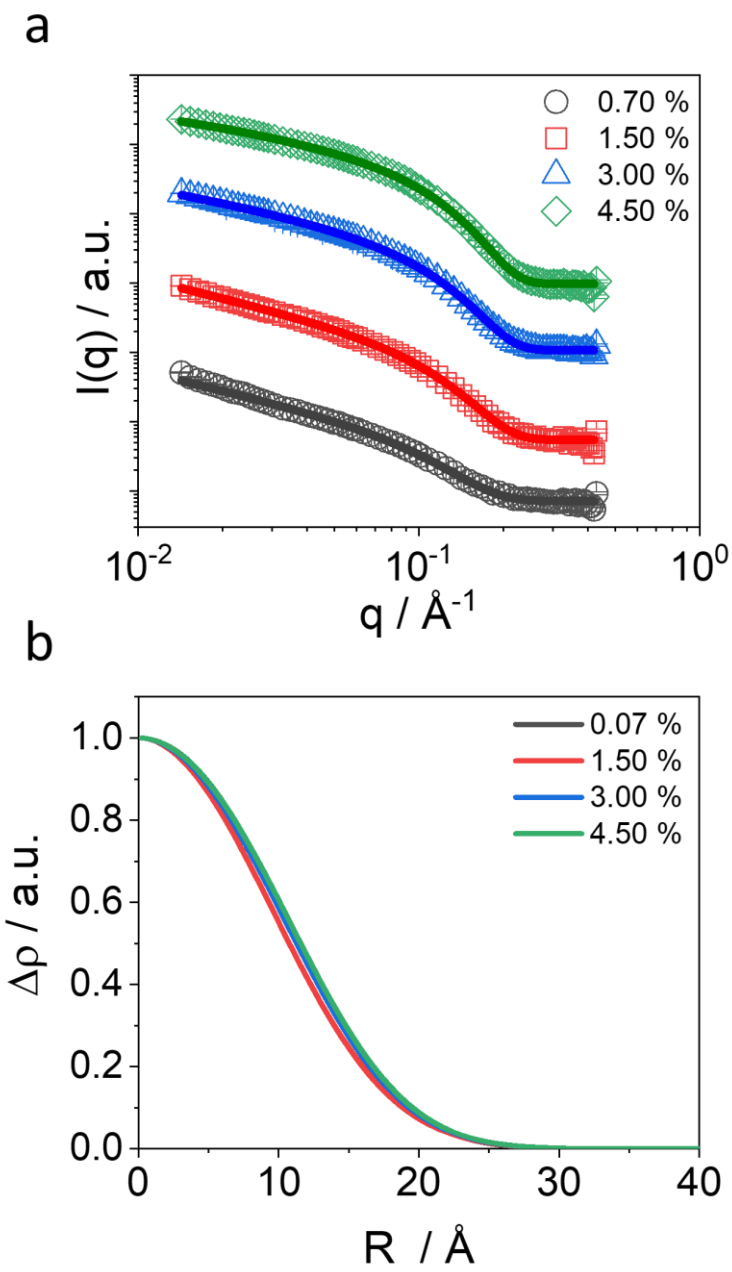

Figure S10. (a) SAXS curves for 0.7, 1.50, 3.00, and 4.50% (w/v) BEAQ-gel. The gray, red, blue, and green lines denote the fitting of diffuse cylinder model. The curves were shifted vertically for easier visualization (b) Radial electron density profile of the cylinders.

Table S5. Obtained parameters from fitting the SAXS curves for 0.7, 1.50, 3.00, and 4.5% BEAQ gel with a diffuse cylinder model.

Sample / %	R_c **/ Å**	σ_{int}**/ Å**	***L* / Å**	σ_c / R_c **(%)**	ν
0.70	11.7 ± 0.8	6.5 ± 0.6	7000 ± 1500	~1	0.0
1.50	11.8 ± 0.8	6.2 ± 0.6	6000 ± 1500	~1	0.0
3.00	12.2 ± 0.8	6.3 ± 0.6	4000 ± 1000	~1	0.11 ± 6
4.50	12.0 ± 0.8	6.4 ± 0.6	1200 ± 300	~1	0.17 ± 7

15. Xanthan gum polymer: Structure and gel photograph

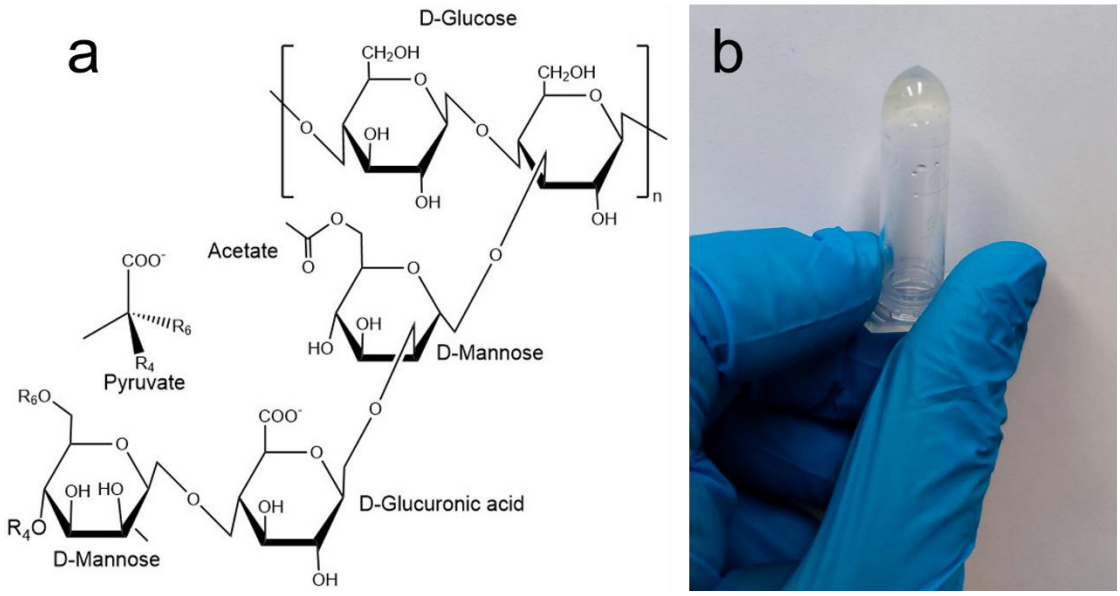

Figure S11. (a) Xanthan gum chemical structure and (b) image of ferricyanide-XG-gel.

16. Photographs of the assembled battery

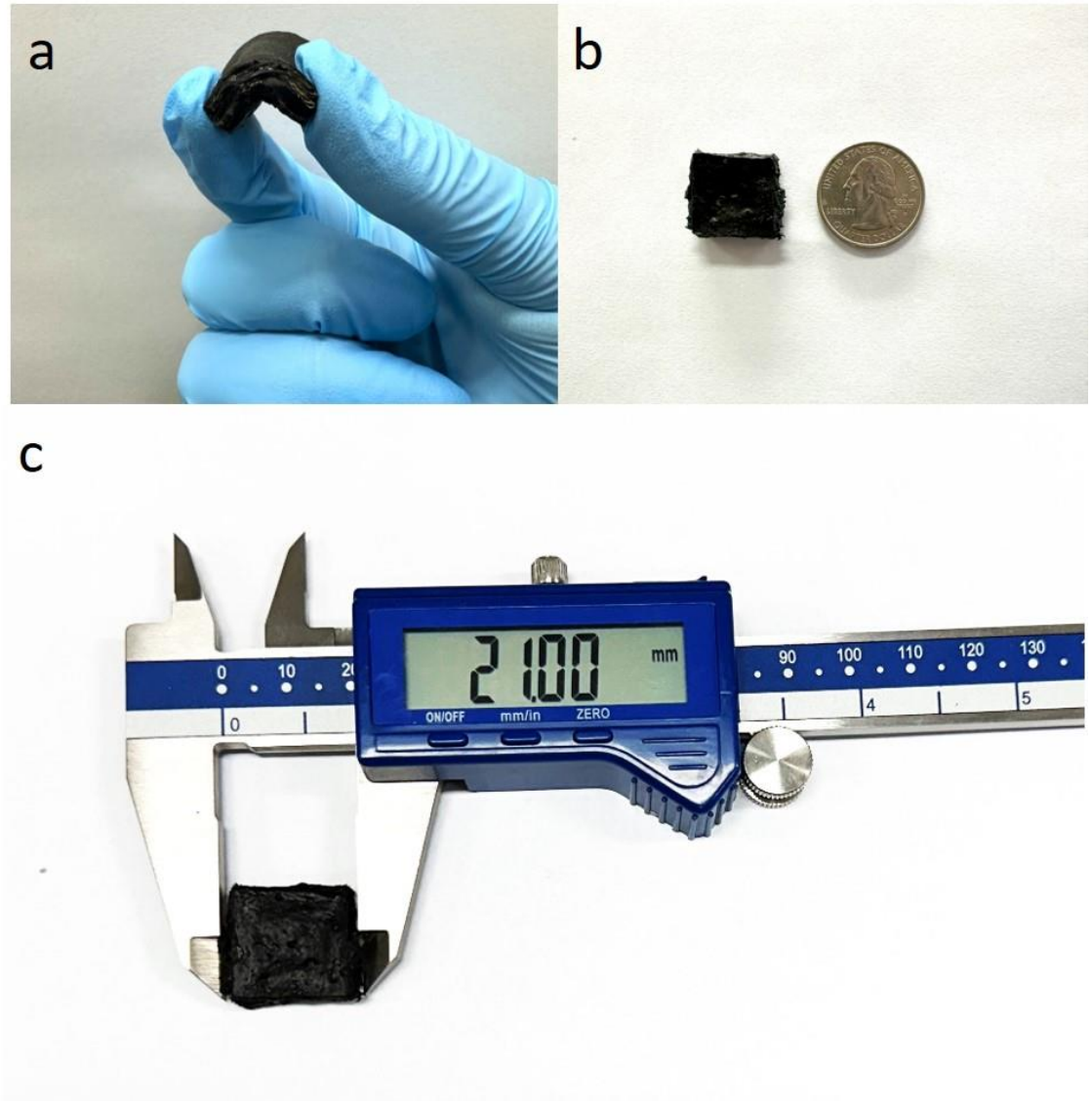

Figure S12. (a) Photograph of the developed microbattery being bent, (b) and (c) size comparison and measurement of the battery with a coin of quarter-dollar and using the pachymeter, respectively.

17. Conductivity calculations

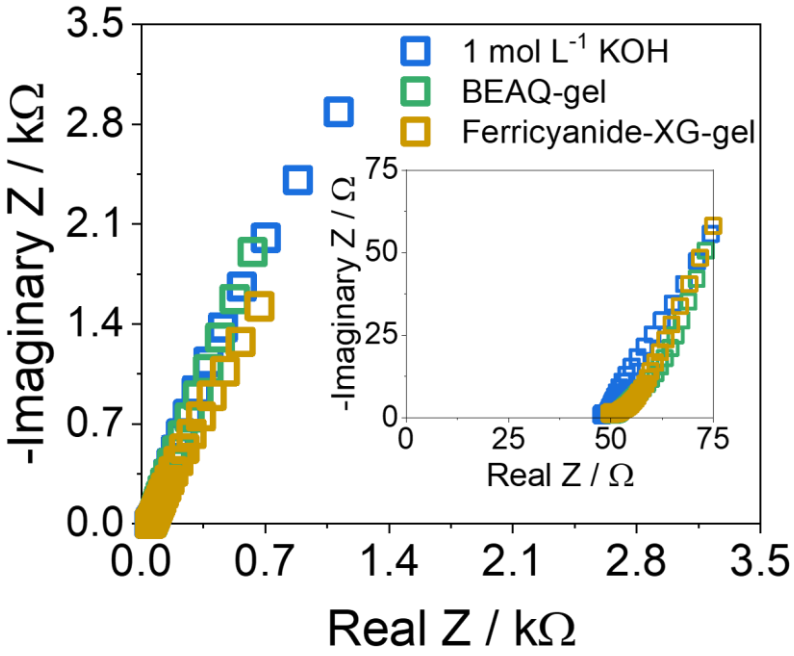

Figure S13. Nyquist plots of clean 1.0 mol L^{-1} KOH solution, BEAQ-gel (1.5 % (w/v) in 1.0 mol L^{-1} KOH), and ferricyanide-XG-gel (0.2 mol L^{-1} $K_4[Fe(CN)_6]$ in 1.0 mol L^{-1} KOH and 40 mg mL^{-1} xanthan gum). The inset figure shows the intersect with x-axis.

Table S6. Calculated conductivities for 1.0 mol L^{-1} KOH, ferricyanide-XG-gel, BEAQ-gel. The reported values are an average of three measurements.

Sample	Average Conductivity / S cm^{-1}
1.0 mol L^{-1} KOH	0.106 ± 0.028
ferricyanide-XG-gel	0.121 ± 0.015
BEAQ-gel	0.143 ± 0.015

18. Comparison of conductivities of gels employed in battery applications.

Table S7. Comparison of conductivities among some reported hydrogel electrolytes applied in battery research.

Hydrogel	Conductivity / mS cm^{-1}	References
SAS10	0.013*	[18]
SPI/PAAM	0.058	[19]
PAAm/HNTs	0.027	[20]
CT3G30	0.038**	[21]
30 kGy RTMS-PVA	0.071	[22]
PCZ-gel	0.027	[23]
BEAQ-gel	0.121	This work
Ferricyanide-XG-gel	0.125	This work

*Conductivity at 20°C
*Conductivity at 60°C

19. Development of a U-shaped platform for bent battery measurements

To perform the experiments in 180° we developed a U-shaped 3D printed form capable of hosting the battery bent during several hours. We designed the form using Tinkercad (AutoDesk) online software and printed it in acrylonitrile-butadiene-styrene (ABS) copolymer in a GTMax Core A1 Dual 3D printer (GTMax 3D, Brazil). The surface finishing took place by inserting the just printed form in acetone until the surface becomes smooth. **Figure S13** shows front and side images of the battery inserted in the U-shaped device and demonstrate the bent mode used during the electrochemical measurements.

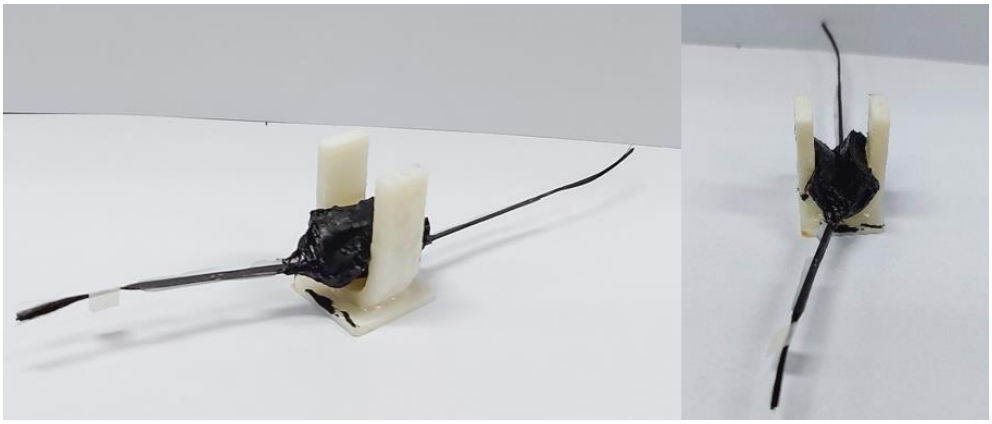

Figure S14. Front and side images of the BEAQ-gel coupled Ferricyanide-XG-gel wearable battery inserted in the 3D printed device at 180° bent conformation.

20. Electrochemical characterization of the battery in larger size

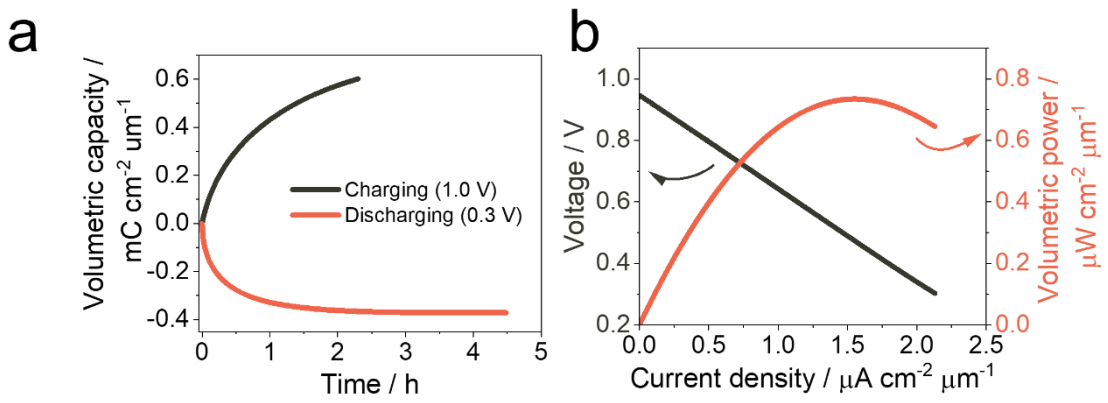

Figure S15. (a) Charging at 1.0 V (black) and discharging at 0.3 V (red) curves and (b) current-voltage (black) and power (red) curves. All measurements took place with the bigger size battery in 180° bent conformation and nitrogen atmosphere.

21. Comparison of the BEAQ-gel vs Ferricyanide battery and previously published microbatteries

Table S8. Comparison of performance among the developed 2-BEAQ-based microbattery and previously published works.

Battery Description	Voltage / V	Power / μW cm^{-2}	Power / μW cm^{-2} $μm^{-1}$	Areal Capacity / μAh cm^{-2}	Volumetric capacity / μAh cm^{-2} $μm^{-1}$	Reference
Quasi-solid -state zinc-ion	-	67.2	-	160	-	[24]
Multilayer graphene battery	-	-	-	6.2	-	[25]
Li-ion	-	-	-	3.5 / 370[2]	-	[26]
Li-ion	-	-	-	10.6	-	[27]
BTMAP-Vi / BTMAP-Fc	0.70		3.4	-	0.39	[28]
BEAQ-gel / Ferricyanide	0.89 / 0.95[3]	-	1.17	119.5	0.06	This work

[1] Areal capacity of First cycle / At 20 C
[2] Areal capacity in Planar assembly / 3D electrode assembly
*The battery in larger size.

22. References

[1] A. R. Pereira, J. C. P. P. de Souza, R. M. Iost, F. C. P. F. P. F. Sales, F. N. Crespilho, *Journal of Electroanalytical Chemistry* **2016**, *780*, 396.

[2] S. I. Bailey, I. M. Ritchie, F. R. Hewgill, *Journal of the Chemical Society, Perkin Transactions 2* **1983**, 645.

[3] P. J. Celis-Salazar, C. C. Epley, S. R. Ahrenholtz, W. A. Maza, P. M. Usov, A. J. Morris, *Inorganic Chemistry* **2017**, *56*, 13741.

[4] A. Hammersley, *Journal of Applied Crystallography* **2016**, *49*, 646.

[5] C. L. P. Oliveira, T. Vorup-Jensen, C. B. F. Andersen, G. R. Andersen, J. S. Pedersen, (Eds.: Gomez, M.; Nogales, A.; Garcia-Gutierrez, M. C.; Ezquerra, T. A.), Springer Berlin Heidelberg, Berlin, Heidelberg, **2009**, pp. 231–244.

[6] M. Kotlarchyk, S. Chen, *The Journal of Chemical Physics* **1983**, *79*, 2461.

[7] T. Neugebauer, *Ann Physik: Berlin* **1943**, *42*, 509.

[8] J. S. Pedersen, *Advances in Colloid and Interface Science* **1997**, *70*, 171.

[9] A. Sundblom, C. L. P. Oliveira, A. E. C. Palmqvist, J. S. Pedersen, *The Journal of Physical Chemistry C* **2009**, *113*, 7706.

[10] E. S. Beh, D. De Porcellinis, R. L. Gracia, K. T. Xia, R. G. Gordon, M. J. Aziz, *ACS Energy Letters* **2017**, *2*, 639.

[11] Y. Ji, M.-A. A. Goulet, D. A. Pollack, D. G. Kwabi, S. Jin, D. De Porcellinis, E. F. Kerr, R. G. Gordon, M. J. Aziz, *Advanced Energy Materials* **2019**, *9*, 1900039.

[12] K. Lin, Q. Chen, M. R. Gerhardt, L. Tong, S. B. Kim, L. Eisenach, A. W. Valle, D. Hardee, R. G. Gordon, M. J. Aziz, M. P. Marshak, *Science* **2015**, *349*, 1529.

[13] S. Jin, E. M. Fell, L. Vina-Lopez, Y. Jing, P. W. Michalak, R. G. Gordon, M. J. Aziz, *Advanced Energy Materials* **2020**, *10*, 2000100.

[14] M. Wu, Y. Jing, A. A. Wong, E. M. Fell, S. Jin, Z. Tang, R. G. Gordon, M. J. Aziz, *Chem* **2020**, *6*, 1432.

[15] Y. Jing, E. M. Fell, M. Wu, S. Jin, Y. Ji, D. A. Pollack, Z. Tang, D. Ding, M. Bahari, M.-A. Goulet, T. Tsukamoto, R. G. Gordon, M. J. Aziz, *ACS Energy Lett* **2022**, *7*, 226.

[16] D. L. Pavia, G. M. Lampman, G. S. Kriz, J. A. Vyvyan, *Introduction to spectroscopy*, Cengage learning, **2014**.

[17] L. Martínez, R. Andrade, E. G. Birgin, J. M. Martínez, *J Comput Chem* **2009**, *30*, 2157.

[18] C. Yuan, X. Zhong, P. Tian, Z. Wang, G. Gao, L. Duan, C. Wang, F. Shi, *ACS Appl Energy Mater* **2022**, *5*, 7530.

[19] D. Jiang, N. Lu, L. Li, H. Zhang, J. Luan, G. Wang, *J Colloid Interface Sci* **2022**, *608*, 1619.

[20] P. Shen, Y. Hu, S. Ji, H. Luo, C. Zhai, K. Yang, *Colloids Surf A Physicochem Eng Asp* **2022**, *647*, 129195.

[21] M. Chen, J. Chen, W. Zhou, X. Han, Y. Yao, C.-P. Wong, *Advanced Materials* **2021**, *33*, 2007559.

[22] Z. Wang, K. Sheng, Z. Zhou, H. Li, Z. Zhang, M. Xiong, J. Huang, *Radiation Physics and Chemistry* **2023**, *204*, 110682.

[23] H. Zhang, X. Gan, Z. Song, J. Zhou, *Angewandte Chemie International Edition* **2023**, *62*, e202217833.

[24] Y. Zhou, W. Li, Y. Xie, L. Deng, B. Ke, Y. Jian, S. Cheng, B. Qu, X. Wang, *ACS Appl Mater Interfaces* **2023**, *15*, 9486.

[25] H. Murata, Y. Nakajima, Y. Kado, N. Saitoh, N. Yoshizawa, T. Suemasu, K. Toko, *ACS Appl Energy Mater* **2020**, *3*, 8410.

[26] M. Létiche, E. Eustache, J. Freixas, A. Demortière, V. De Andrade, L. Morgenroth, P. Tilmant, F. Vaurette, D. Troadec, P. Roussel, T. Brousse, C. Lethien, *Adv Energy Mater* **2017**, *7*.

[27] H.-S. Min, B. Y. Park, L. Taherabadi, C. Wang, Y. Yeh, R. Zaouk, M. J. Madou, B. Dunn, *J Power Sources* **2008**, *178*, 795.

[28] F. N. Crespilho, G. C. Sedenho, D. De Porcellinis, E. Kerr, S. Granados-Focil, R. G. Gordon, M. J. Aziz, *J Mater Chem A Mater* **2019**.